Studies on Electrical Conduction Characteristics of Metal/Molecule/Metal Nanoscale Junction Device

金属/分子/金属ナノスケール接合素子の電気伝導特性に関する研究

Takahiro Misawa

Graduate School of Chemical Sciences and Engineering
Hokkaido University

2017

Contents

Chapter 1

General Introduction

1.1 Spintronics

Spintronics is an emerging research field which aims to create novel electronics by utilizing the charge and spin degrees of freedom of electrons in solid-state systems. This research field enabled us to observe a lot of interesting fundamental phenomena, such as giant magnetoresistance (GMR) [1,2], tunnel magnetoresistance (TMR) [3−9], spin filter effect [10−14], and spin Hall effect [15,16]. Recently, these excellent characteristics are received much attention from the aspects of practical applications in magnetic sensors, magnetic heads in hard disc drive (HDD), and magnetic random access memories (MRAMs) [17,18]. From such fundamental and practical perspectives, spintronics is expected as a next-generation electronics utilizing spin.

In the field of spintronics, one of the most important phenomena is the TMR effect. This effect is observed in magnetic tunnel junctions (MTJs), which consist of two ferromagnetic (FM) layers separated by a thin insulator (Figure 1.1). When the thickness of the insulator is thin at a few nanometers, the tunnel current flows. In this situation, when the magnetizations of FM layers are parallel, the resistance is small, and when the magnetizations of FM layers are antiparallel, the resistance is large. Since the magnetization configuration can be controlled by magnetic field, the resistance can change depending on the magnetic field. The change of resistance in accordance with the relative orientation of two FM layers is called the TMR effect. The resistance changing ratio is defined by

$$TMR\ ratio = \frac{\Delta R}{R} = \frac{R_{\mathrm{AP}} - R_{\mathrm{P}}}{R_{\mathrm{P}}}, \tag{1.1}$$

where $R_{P(AP)}$ is a resistance of the parallel (antiparallel) configuration. The equation (1.1) is a figure of merit of magnetic sensitivity. According to the Julliere formula [19], the TMR ratio can be expressed by

$$TMR\ ratio = \frac{2P_{FM1}P_{FM2}}{1-P_{FM1}P_{FM2}}, \tag{1.2}$$

where P_{FM1} and P_{FM2} are respectively spin polarization of FM1 and FM2 layers (Figure 1.2). Here, the spin polarization is given by

$$P_{\xi} = \frac{D_{\xi,\uparrow}(E_F) - D_{\xi,\downarrow}(E_F)}{D_{\xi,\uparrow}(E_F) + D_{\xi,\downarrow}(E_F)}, \tag{1.3}$$

where ξ denotes the layer number of FM layer, and $D_{\xi,\uparrow}(E_F)$ and $D_{\xi,\downarrow}(E_F)$ are the density of states (DOS) of the ξ layer at the Fermi energy (E_F) for majority-spin and minority-spin electrons, respectively. From the equations (1.2) and (1.3), it is found that a large TMR ratio can be obtained for a high spin polarization of two FM layers.

Many researchers made a great effort to increase the TMR ratio based on Julliere's theory. Since a TMR of 18% was discovered in MTJs using Al-oxide tunnel barrier in 1995 [3,4], a TMR increased up to 70% using Al-oxide-based MTJs. Then, in 2004, a giant TMR over 200% was observed in MTJs using crystalline MgO tunnel barrier [5,6]. According to the band calculation, a giant TMR was predicted in MgO-based MTJs due to the coherent tunneling, enabling a high spin polarization of tunneling current. Yuasa *et al.* and Parkin *et al.* demonstrated a giant TMR in such MgO-based MTJs. At present, a TMR reached up to 600% in MgO-based MTJs [9].

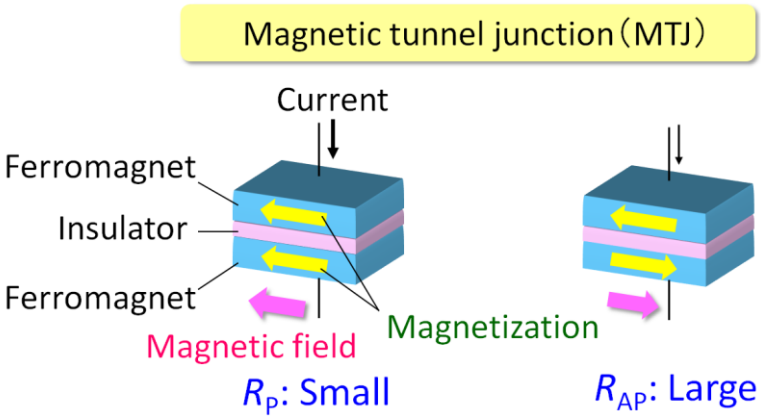

Figure 1.1 TMR effect in MTJs, which consist of two FM layers separated by a thin insulator. When the magnetizations of FM layers are parallel, the resistance is small, and when the magnetizations of FM layers are antiparallel, the resistance is large.

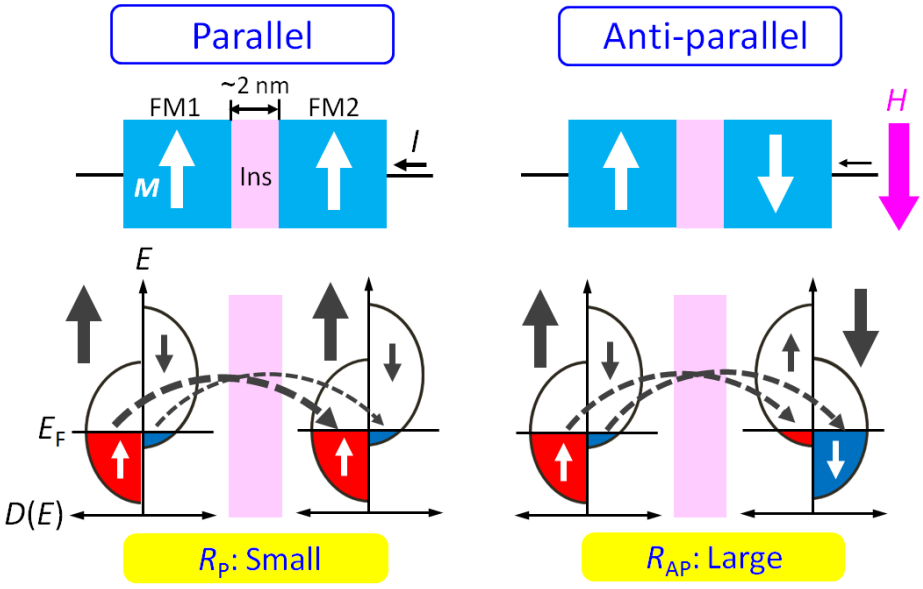

Figure 1.2 Mechanism of TMR effect.

1.2 Molecular spintronics

Researches in organic semiconductors (OSCs) have progressed considerably over the past few decades [20]. The greatest success has been achieved in the field of optoelectronics. Display products using organic light-emitting diodes (OLEDs) have become available to consumers, and the field in organic photovoltaic devices is becoming as one of the challenging research topics toward

the commercial applications. Remarkable improvements have also been achieved in the field of organic field-effect transistors (OFETs), and fundamental works based on OFETs have progressed to realize organic electric memories for data storage applications.

OSCs have recently paid the attention of researchers in spintronics, and significant efforts are being made towards the integration between OSCs and spintronics [21,22]. Xiong *et al.* achieved observation a large magentoresistance (MR) effect of 40% at 11 K in $La_{0.67}Sr_{0.33}MnO_3$/ tris(8-hydroxy-quinolinato) aluminum (Alq_3)/Co molecular spin valve devices (Figure 1.3 [23]). Subsequently, Santos *et al.* obtained an MR ratio of 7.5% at 4.2 K and 4.6% at room temperature in $Co/Al_2O_3/Alq_3/NiFe$ junctions (Figure 1.4) [24]. In other groups, a large MR effect has also been observed in $La_{0.7}Sr_{0.3}MnO_3/Alq_3/Al_2O_3/Co$ [25], Co/4,4'-bis99-(ethyl-3-carbazovinylene)-1,1'-biphenyl (CVB)/$La_{0.67}$ $Sr_{0.33}MnO_3$ [26], and $La_{0.67}Sr_{0.33}MnO_3$/tetraphenyl porphyry (TPP)/Co [27]. In addition to this feature, the increase of a spin-relaxation time has also been one of the most attractive aspects for OSCs. This enhancement is attributed to the low spin-orbit coupling in OSCs.

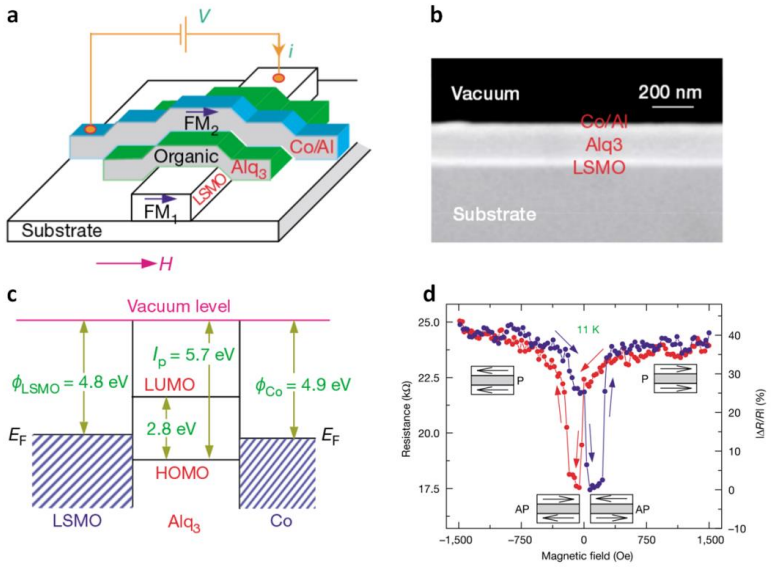

Figure 1.3 $La_{0.67}Sr_{0.33}MnO_3/Alq_3/Co$ molecular spin valve devices (Ref. 23). (a) Schematic device structure. (b) Cross-sectional SEM image of stacked structure. (c) Energy diagram of $La_{0.67}Sr_{0.33}MnO_3/Alq_3/Co$. (d) MR effect of device.

The spin–orbit interaction H_{so} is given by

$$H_{SO} = \frac{\mu_0}{4\pi}\frac{Z^4 e^2}{2m^2}\frac{\hbar}{a_0^3 n^6}(\hbar l \cdot s), \tag{1.4}$$

where μ_0 is the magnetic permeability of vacuum, ε_0 is the permittivity of vacuum, Z is the atomic number, e is the electric charge, m is the mass of electrons, $\hbar$ is the Planck constant divided by 2π, a_0 is the Bohr radius, n is the principal quantum number, l is the orbital angular momentum, and s is the spin angular momentum. According to the equation (1.4), the spin-orbit interaction strength is proportional to Z^4. Carbon has a low atomic number (Z), indicating a weak spin-orbit interaction. Such weak interaction achieves a long spin-relaxation time in excess of 10 μs [28,29]. A long spin-diffusion length has also been observed. Representative results on spin-relaxation times and spin-diffusion length are shown in Table 1.1.

1.3 Nanoscale junctions

Recent progress of metal- and molecule-based nanoscale junctions has led to the observation of fascinating physical/chemical phenomena, such as conductance quantization [39,40], electrical switching/rectification [41,42], enhanced thermoelectric effect [43], and extremely large MR [44] (Figure 1.5). For example, the conductance in metal nanoscale junctions is quantized by the integer times of $2e^2/h$, where e is the electron charge and h is the Planck's constant, and that in magnetic nanoscale junctions is characterized by the half-integer times of $2e^2/h$. Electrical switching or rectification properties are also observed in metal/self-assembled monolayer (SAM)/metal nanoscale junctions due to the movement of molecules or redox reaction [41]. In another study, the enhancement of Seebeck coefficient has been measured at room temperature in metal/molecule/metal nanoscale junctions, consisting of 1,4-benzenedithiol, 4,4'-dibenzenedithiol, or 4,4''-tribenzenedithiol molecules bridged between two gold electrodes [45]. Moreover, a large MR effect of 300% has been reported at 2 K in $Co/Alq_3/La_{0.7}Sr_{0.3}MnO_3$ nanoscale junctions [44].

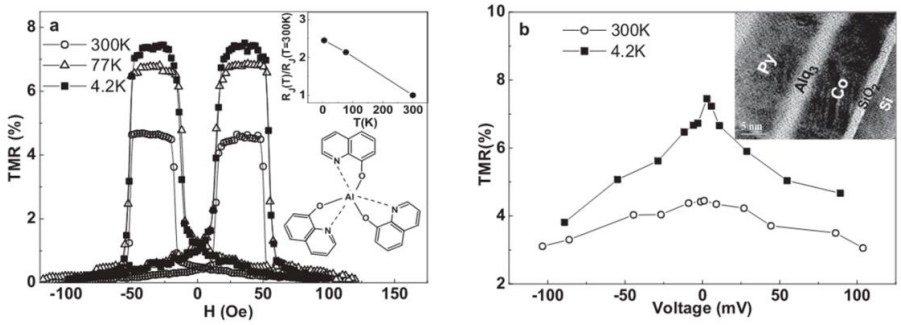

Figure 1.4 $Co/Al_2O_3/Alq_3/NiFe$ junctions (Ref. 24). (a) MR effect of junction at 4.2, 77, and 300 K. Inset shows junction resistance as a function of temperature. (b) Voltage dependence of TMR ratio at 4.2 and 300 K. Inset shows cross-sectional TEM image of stacked structure [24].

Table 1.1 Spin–diffusion length and time in molecular spintronic devices.

Organic semiconductors	Spin-polarized electrodes	Spin-diffusion length L_s (nm) and time T_s(s)
6T 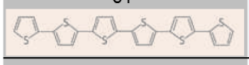	LSMO/LSMO	$L_s \approx 70$ [32,33] $T_s \approx 10^{-6}$
Alq_3 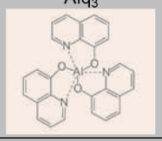	LSMO/Co [25–27,30]	$L_s \approx 100$ [25] $l_s \approx 45$ [23]
	Fe/Co [36, 37]	$T_s \approx 26 \times 10^{-6}$
	Co/Ni [38]	$T_s \approx 10^{-3}$
RRP3HT 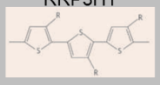	LSMO/Co [30]	$L_s \approx 80$ [30]
	$Fe_{50}Co_{50}/Ni_{81}Fe_{19}$ [34]	
Rubrene 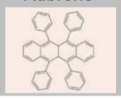	Co/Fe [35]	$L_s \approx 13.3$

Various nanofabrication methods have been proposed to realize nano-junctions, i.e., optical or electron-beam (EB) lithography, integrated bottom-up and top-down processing, and break junction technique [46–52] (Figure 1.6). Immersion lithography performed at 193-nm wavelength has enabled the creation of a 22-nm line-width technology featuring 3-D tri-gate transistors and also demonstrated a 14-nm technology including the second generation Fin Field Effect Transistor architecture [46]. EB lithography with high-contrast development was also found to be capable of producing 10-nm features with sub-20 nm pitches at an acceleration voltage of 10 kV.

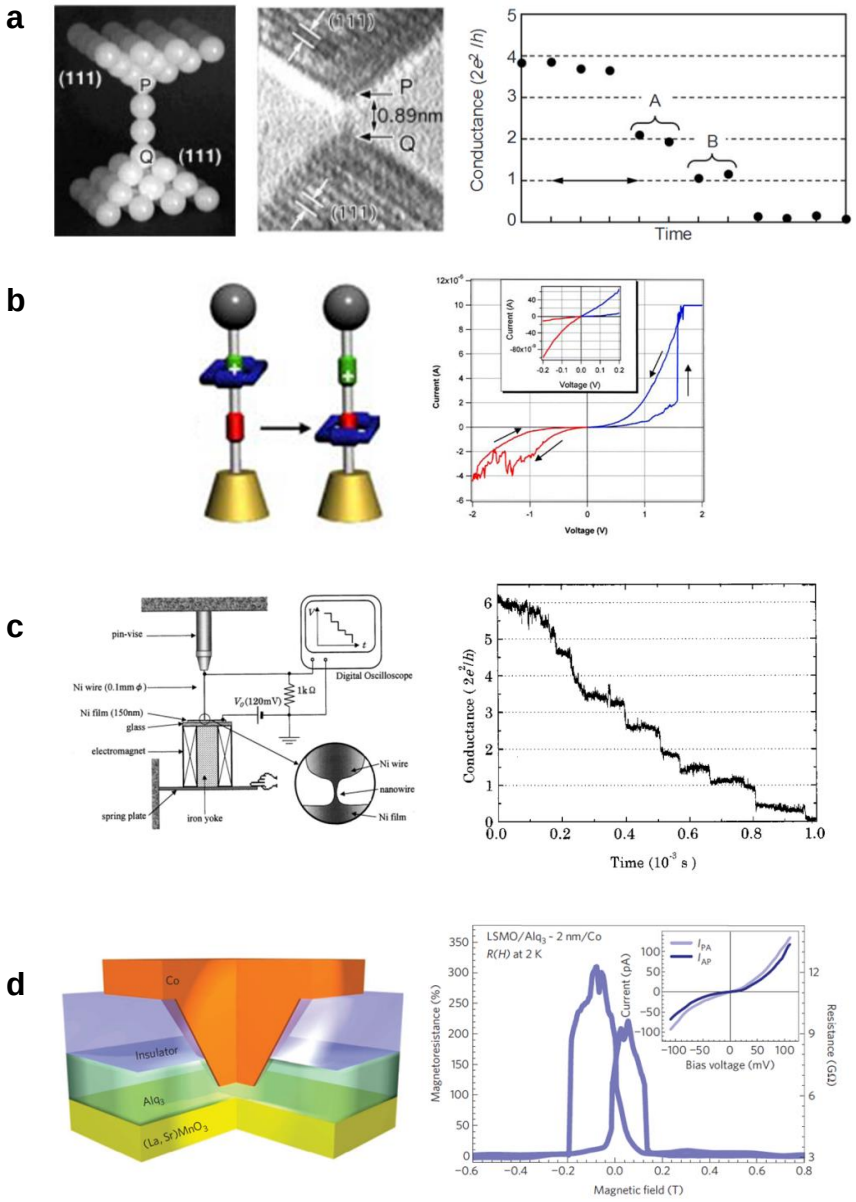

Figure 1.5 Various phenomena in metal- and molecule-based nanoscale junctions. (a) Quantization of conductance in Au nanoscale junctions (Ref. 39), (b) molecular switching in metal/self-assembled monolayer (SAM)/metal junctions (Ref. 41), (c) quantization of spin conductance in Ni junctions (Ref. 40), and (d) large MR effect of Co/Alq_3/$La_{0.7}Sr_{0.3}MnO_3$ junctions (Ref. 44).

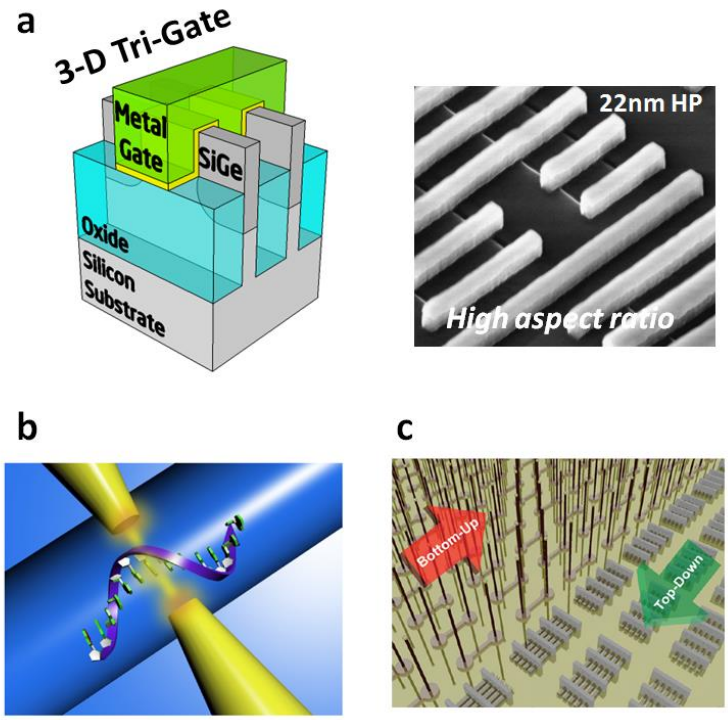

Figure 1.6 Nanostructures fabricated using various methods; (a) immersion lithography (Ref. 46), (b) break junction technique (Ref. 51), and (c) integrated bottom-up and top-down processing (Ref. 52).

Directed self-assembly (DSA) of block copolymer (BCP) thin films, in which the obtained nanoscale line/pitch features are defined by the spacer/width of the aligned BCPs fabricated using EB lithography combined with DSA, was used to produce long range ordered Si nanofins with 10-nm sizes and 32-nm pitches [52]. The superlattice nanowire pattern transfer method, which is based on the stamp formation due to the selective etching of superlattice template layers, has also enabled the production of Pt and Si nanowires with sub-10-nm widths and sub-15-nm pitches [50].

Recently, our group have proposed a new method to fabricate nanoscale junctions utilizing thin-film edges, in which molecules are sandwiched between crossed edges of two metal thin films, where the junction area is determined by the precisely controlled film thickness (Figure 1.7). Namely, the films with thicknesses of 1–20 nm could produce nanoscale junctions with

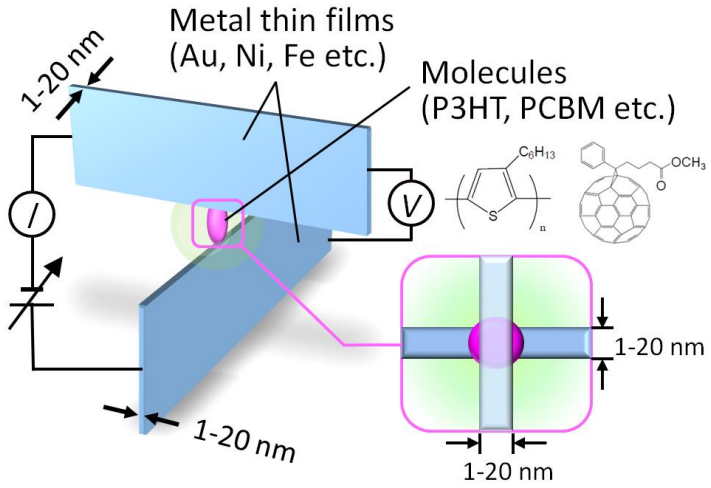

Figure 1.7 Schematic of metal/molecule/metal nanoscale junction containing metal thin-film edges. Nanoscale junction consists of molecules sandwiched between crossed edges of two metal thin films. Junction area is determined by film thickness; thus, 1−20-nm thick films could produce 1×1–20×20-nm^2 nanoscale junctions.

areas of 1×1–20×20 nm^2. This geometrical structure also enables a strict junction resistance measurement, i. e., the resistance of molecules, using four probe method. Moreover, the electrode resistance fabricated from metal thin films can be reduced to several 10–100 Ω due to high aspect ratios of electrode (typically over 10^5:1). Such a reduction in resistance is characterized by the following advantages: i) high-speed operation due to small time constant value proportional to electrode resistance; and ii) low energy consumption due to the suppression of heat generation originated from large magnitude of electrode resistance. Furthermore, a large MR effect is expected from the nanostructures of magnetic thin film electrode. In particular, such nanojunctions utilizing magnetic thin films are called as spin quantum cross (SQC) devices.

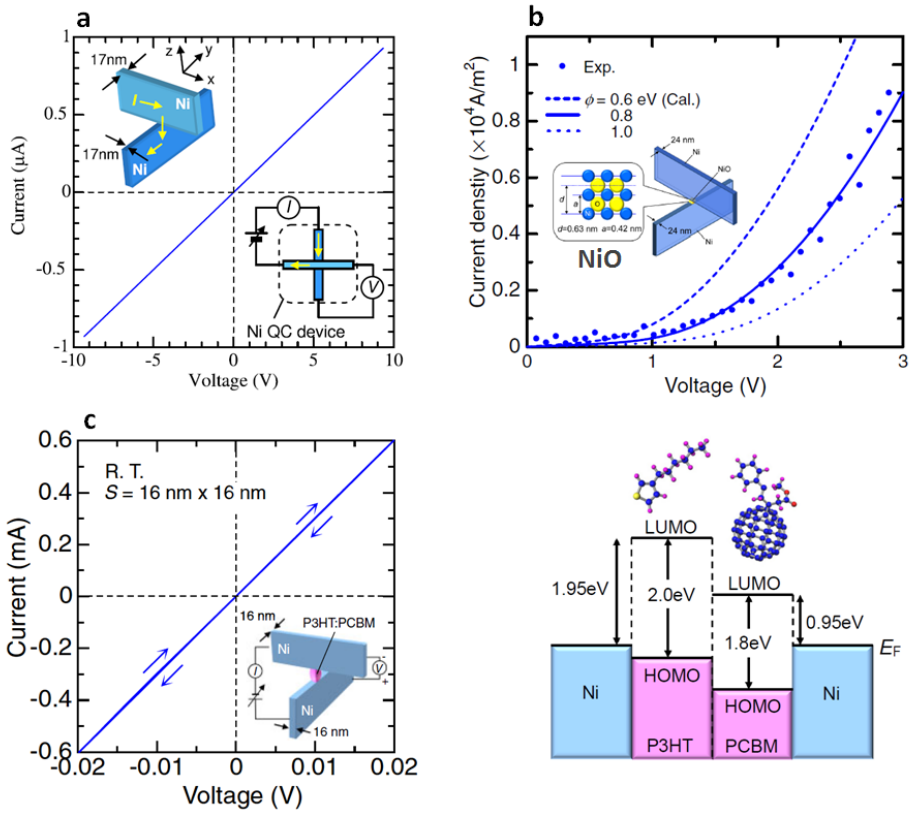

Figure 1.8 (a) Ohmic characteristics of Ni/Ni junctions [54], (b) nanoscale tunnelling observed for Ni/NiO/Ni junctions [55], and (c) ballistic regime of nanoscale molecules in Ni/P3HT:PCBM/Ni nanoscale junctions [56].

Previously, our research group have fabricated Ni-based nanoscale junctions utilizing thin-film edges and investigated the related nanoscale phenomena [53–56]. The obtained results include ohmic characteristics of Ni/Ni junctions, nanoscale tunnelling observed for Ni/NiO/Ni junctions, and the ballistic regime of nanoscale molecules in Ni/poly-3-hexylthiophene:6, 6-phenyl C61-butyric acid methyl ester (P3HT:PCBM)/Ni nanoscale junctions (Figure 1.8). To fabricate such nanoscale junctions, poly(ethylene naphthalate) (PEN) organic films were used as substrates. However, these films limit the process flexibility due to their low glass transition temperature (T_g) as high as 120°C. Namely, it was difficult to anneal the nanoscale junctions at higher than 120°C for surface/interface engineering and crystal structure optimization. In addition, PEN films are

impractical for typical manufacturing process, such as a CMOS–LSI one requiring thermal treatment. Moreover, the magnetic measurement revealed a small coercive force and a low squareness of hysteresis loop for the magnetic thin films grown on PEN films.

1.4 Aim of this study

This study proposes a new fabrication technique utilizing thin-film edges toward the creation of molecular spintronic nanoscale junctions. In particular, I attempted to use low-softening-point (LSP) glasses as substrates with excellent thermal processability instead of conventional PEN films. A thermal pressing technique was used for the formation of LSP-glass/magnetic-thin-film/LSP-glass sandwiched structures. Structural, electrical, and magnetic properties were investigated for magnetic thin films on LSP glasses and in the sandwiched structures. Nanoscale junctions were fabricated, in where molecules were sandwiched between crossed edges of two magnetic thin films. Their current-voltage characteristics were investigated. Finally, the carrier transport properties of the junctions were discussed within the areas ranging from nanometer to micrometer scale.

This thesis consists of five chapters. Chapter 1 presents a review of the background and describes the significance and objectives of this study.

In chapter 2, the formation of Co thin films sandwiched between LSP glasses was demonstrated using a thermal pressing process. Structural and magnetic properties were investigated for Co thin-film electrodes on LSP glasses and Co thin films sandwiched between the glasses.

In chapter 3, structural and magnetic properties were investigated for $Ni_{78}Fe_{22}$ thin films on LSP glasses and $Ni_{78}Fe_{22}$ thin films sandwiched between the glasses. The influence of thermal pressing process on the characteristics of $Ni_{78}Fe_{22}$ thin films sandwiched between LSP glasses was revealed. The stray magnetic field generated between the two edges of $Ni_{78}Fe_{22}$ thin-film electrodes

in nanoscale junctions was calculated using a micromagnetic simulation. Finally the applicability to spin-filter devices was discussed.

In chapter 4, the formation of nanoscale junctions, consisting of Alq_3 molecules sandwiched between crossed edges of two $Ni_{78}Fe_{22}$ thin films, was demonstrated. This technique enabled the fabrication of $Ni_{78}Fe_{22}/Alq_3/Ni_{78}Fe_{22}$ junctions with an area of 11×11 nm^2, which is the smallest value ever reported junctions utilizing thin-film edges. Area dependence of electrical properties of $Ni_{78}Fe_{22}/Alq_3/Ni_{78}Fe_{22}$ junctions was investigated from nanometer to micrometer scale. Consequently, a bridging area was found out between the quantum state and classical configuration.

Finally, all the results and achievements of this study are summarized in chapter 5.

The result of this study is expected to open the window for the discovery of various physical/chemical phenomena in nano-to-micro-scale materials, and offer new opportunities for the creation of next-generation innovative nanodevices.

1.5 References

1. M. N. Baibich, J. M. Broto, A. Fert, F. Nguyen Van Dau, F. Petroff, P. Eitenne, G. Creuzet, A. Friederich, and J. Chazelas, *Phys. Rev. Lett.* **61** (1988) 2472.
2. G. Binasch, P. Griinberg, F. Saurenbach, and W. Zinn, *Phys. Rev. B* **39** (1989) 4828.
3. T. Miyazaki and N. Tezuka, *J. Magn. Magn. Mater.* **139** (1995) L231.
4. J. S. Moodera, L. R. Kinder, T. M. Wong, and R. Meservey, *Phys. Rev. Lett.* **74** (1995) 3273.
5. S. Yuasa, T. Nagahama, A. Fukushima, Y. Suzuki, and K. Ando, *Nat. Mater.* **3** (2004) 868.
6. S. S. Parkin, C. Kaiser, A. Panchula, P. M. Rice, B. Hughes, M. Samant, and S. H. Yang, *Nat. Mater.* **3** (2004) 862.
7. W. H. Butler, X. G. Zhang, T. C. Schulthess, and J. M. MacLaren, *Phys. Rev. B* **63** (2001) 054416.
8. J. Mathon and A. Umersky, *Phys. Rev. B* **63** (2001) 220403R.
9. S. Ikeda, J. Hayakawa, Y. Ashizawa, Y. M. Lee, K. Miura, H. Hasegawa, M. Tsunoda, F. Matsukura, and H. Ohno, *Appl. Phys. Lett.* **93** (2008) 082508.
10. J. S. Moodera, X. Hao, G. A. Gibson, and R. Meservey, *Phys. Rev. Lett.* **61** (1988) 637.
11. T. Koga, J. Nitta, H. Takayanagi, and S. Datta, *Phys. Rev. Lett.* **88** (2002) 126601.
12. A. Slobodskyy, C. Gould, T. Slobodskyy, C. R. Becker, G. Schmidt, and L. W. Molenkamp, *Phys. Rev. Lett.* **90** (2003) 246601.
13. J. S. Moodera, T. S. Santos, and T. Nagahama, *J. Phys.: Condens. Matter* **19** (2007) 165202.
14. T. Nagahama, T. S. Santos, and J. S. Moodera, *Phys. Rev. Lett.* **99** (2007) 016602.
15. J. E. Hirsch, *Phys. Rev. Lett.* **83** (1999) 1834.
16. Y. K. Kato, R. C. Myers, A. C. Gossard, D. D. Awschalom, *Science* **306** (2004) 1910.
17. H. Yoda, T. Kishi, T. Nagase, M. Yoshikawa, K. Nishiyama, E. Kitagawa, T. Daibou, M. Amano, N. Shimomura, S. Takahashi, T. Kai, M. Nakayama, H. Aikawa, S. Ikegawa, M.

Nagamine, J. Ozeki, S. Mizukami, M. Oogane, Y. Ando, S. Yuasa, K. Yakushiji, H. Kubota, Y. Suzuki, Y. Nakatani, T. Miyazaki, and K. Ando, *Curr. Appl. Phys.* **10** (2010) e87.

18. N. Nishimura, T. Hirai, A. Koganei, T Ikeda, K. Okano, Y. Sekiguchi, and Y Osada, *J. Appl. Phys.* **91** (2002) 5246.
19. M. Julliere, *Phys. Lett. A* **54** (1975) 225.
20. R. H. Friend, R. W. Gymer, A. B. Holmes, J. H. Burroughes, R. N. Marks, C. Taliani, D. D. C. Bradley, D. A. Dos Santos, J. L. Brédas, M. Lögdlund, and W. R. Salaneck, *Nature* **397** (1999) 121.
21. W. J. M. Naber, S. Faez, and W. G. van der Wiel, *J. Phys. D: Appl. Phys.* **40** (2007) R205.
22. S. Sanvito, *Nat. Mater.* **6** (2007) 803.
23. Z. H. Xiong, D. Wu, Z. V. Vardeny, and J. Shi, *Nature* **427** (2004) 821.
24. T. S. Santos, J. S. Lee, P. Migdal, I. C. Lekshmi, B. Satpati, and J. S. Moodera, *Phys. Rev. Lett.* **98** (2007) 0166011.
25. V. Dediu, L. E. Hueso, I. Bergenti, A. Riminucci, F. Borgatti, P. Graziosi, C. Newby, F. Casoli, M. P. De Jong, C. Taliani, and Y. Zhan, *Phys. Rev. B* **78** (2008) 1152031.
26. F. J. Wang, C. G. Yang, Z. V. Vardeny, and X. G. Li, *Phys. Rev. B* **75** (2007) 2453241.
27. W. Xu, G. J. Szulczewski, P. LeClair, I. Navarrete, R. Schad, G. Miao, H. Guo, and A. Gupta, *Appl. Phys. Lett.* **90** (2007) 0725061.
28. C. B. Harris, R. L. Schlupp, and H. Schuch, *Phys. Rev. Lett.* **30** (1973) 1019.
29. V. I. Krinichnyi, S. D. Chemerisov, and Y. S. Lebedev, *Phys. Rev. B* **55** (1997) 16233.
30. S. Majumdar, H. S. Majumdar, R. Laiho, and R. Österbacka, *J. Alloys Compd.* **423** (2006) 169.
31. V. A. Dediu, L. E. Hueso, I. Bergenti, and C. Taliani, *Nature Mater.* **8** (2009) 707.
32. V. Dediu, M. Murgia, F. C. Matacotta, C. Taliani and S. Barbanera, *Solid State Commun.* **122** (2002) 181.

33. C. Taliani, V. Dediu, F. Biscarini, M. Cavallini, M. Murgia, G. Ruani, and P. Nozar, *Phase Transitions* **75** (2002) 1049.

34. N. A. Morleya, A. Rao, D. Dhandapani, M. R. J. Gibbs, M. Grell and T. Richardson, *J. Appl. Phys.* **103** (2008) 07F306.

35. J. H. Shim, K. V. Raman, Y. J. Park, T. S. Santos, G. X. Miao, B. Satpati, and J. S. Moodera, *Phys. Rev. Lett.* **100** (2008) 226603.

36. F. J. Wang, Z. H. Xiong, D. Wu, J. Shi, and Z. V. Vardeny, *Synth. Met.* **155** (2005) 172.

37. Y. Liu, S. M. Watson, T. Lee, J. M. Gorham, H. E. Katz, J. A. Borchers, H. D. Fairbrother, and D. H. Reich, *Phys. Rev. B* **79** (2009) 075312.

38. S. Pramanik, C. G. Stefanita, S. Patibandla, S. Bandyopadhyay, K. Garre, N. Harth, and M. Cahay, *Nat. Nanotech.* **2** (2007) 216.

39. H. Ohnishi, Y. Kondo, and K. Takayanagi, *Nature* **395** (1998) 780.

40. T. Ono, Y. Ooka, H. Miyajima, and Y. Otani. *Appl. Phys. Lett.* **75** (1999) 1622.

41. W. Wu, G. Y. Jung, D. L. Olynick, J. Straznicky, Z. Li, X. Li, D.A.A. Ohlberg, Y. Chen, S. Y. Wang, J.A. Liddle, W.M. Tong, and R. S. Williams, *Appl. Phys. A* **80** (2005) 1173.

42. J. Chen, M. A. Reed, A. M. Rawlett, and J. M. Tour, *Science* **286** (1999) 1550.

43. P. Reddy, S. Y. Jang, R. A. Segalman, and A. Majumdar, *Science* **315** (2007) 1568.

44. C. Barraud, P. Seneor, R. Mattana, S. Fusil, K. Bouzehouane, C. Deranlot, P. Graziosi, L. Hueso, I. Bergenti, V. Dediu, F. Petroff, and A. Fert, *Nat. Phys.* **6** (2010) 615.

45. S. V. Aradhya and L. Venkataraman, *Nat. Nanotech.* **8** (2013) 399.

46. C. H. Jan et al. *IEEE Int. Electr. Devices Meeting* (2012) 12-44.

47. S. Natarajan et al. *IEEE Int. Electr. Devices Meeting* (2014) 14-71.

48. J. K.Yang. B. Cord, H. Duan, and K. K. Berggren, *J. Vac. Sci. Technol.* B **27** (2009) 2622.

49. C. Cummins, A. Gangnaik, R. A. Kelly, D. Borah, J. O'Connell, N. Petkov, Y. M. Georgiev, J.

D. Holmes, and M. A. Morris, *Nanoscale* **7** (2015) 6712.

50. J. R. Heath, *Acc. Chem. Res.* **41** (2008) 1609.
51. T. Ohshiro, K. Matsubara, M. Tsutsui, M. Furuhashi, M. Taniguchi and T. Kawai, *Sci. Rep.* **2** (2012) 501.
52. R. G. Hobbs, N. Petkovand, and J. D. Holmes, *Chem. Mater.* **24** (2012) 1975.
53. H. Kaiju, A. Ono, N. Kawaguchi, K. Kondo, A. Ishibashi, J. Won, A. Hirata, M. Ishimaru, Y. Hirotsu, *Appl. Surf. Sci.* **255** (2009) 3706.
54. H. Kaiju, K. Kondo, A. Ono, N. Kawaguchi, J. Won, A. Hirata, M. Ishimaru, Y. Hirotsu, and A. Ishibashi, *Nanotechnology* **21** (2010) 015301.
55. H. Kaiju, K. Kondo, and A. Ishibashi, *Jpn. J. Appl. Phys.* **49** (2010) 105203.
56. H. Kaiju, K. Kondo, N. Basheer, N. Kawaguchi, S. White, A. Hirata, M. Ishimaru, Y. Hirotsu, and A. Ishibashi, *Jpn. J. Appl. Phys.* **51** (2012) 065202.

Chapter 2

Structural and magnetic properties of Co thin films sandwiched between glasses and their application in spin-filter devices

---

2.1 Introduction

Nanoscale junctions can be realized by crossed edges of two ferromagnetic-thin-film electrodes which are formed between glass substrates using a thermal pressing technique. Therefore, the structural and magnetic properties of ferromagnetic-thin-film electrodes are significant to discuss the characteristics of SQC devices such as junction areas, electrical conductivity and stray field. Although there have been many reports on the properties of ferromagnetic thin films deposited on various substrates [1–6], their properties are widely different depending on the kind and/or the purity of substrates. Among them, there is little or no report on the properties of ferromagnetic thin films deposited on B_2O_3-based LSP glasses. In this chapter, it was investigated the structural and magnetic characteristics of the Co thin films on LSP glasses and the films sandwiched between LSP glasses. The stray field between crossed edges of two Co thin-film electrodes was also calculated using a micromagnetic simulation for the SQC device application.

2.2 Experimental

2.2.1 Fabrication of Co film on glass substrate

Figure 2.1 shows the fabrication method of the glass/Co/glass structure. A B_2O_3-based LSP glass (ISUZU GLASS CO., LTD.) was used for the substrate. The LSP glass composition was SiO_2–B_2O_3–Al_2O_3–Na_2O–CaO. The LSP glass deformation temperature was 503°C. The LSP glasses were cut to 10×10×2 mm^3 and polished to a shape with chamfered edges as shown in Figure 2.1(a). The LSP glasses were cleaned in an ultrasonic bath with acetone and ethanol for 10 min, respectively. Afterwards, Co thin films with the thickness of 5–25 nm were deposited on the LSP glasses using an electron beam evaporation (Figure 2.1(b)). During film deposition, the magnetic field of 400 Oe was applied in the in-plane transverse direction of the Co thin films for the induced magnetic anisotropy formation. The base pressure before deposition was 2.5−4.0×10^{-4} Pa. The deposition rate of Co thin films was 0.15 nm/s at an evaporation power of 200 W (4.0 kV and 50 mA). For comparison, the Co thin films were also fabricated on the PEN organic film substrates (Teonex Q65, Teijin DuPont). Co was deposited on the PEN of 10 mm×2 mm×25 μm using the electron beam evaporation under a magnetic field in a high vacuum chamber at a base pressure of ~10^{-6} Pa. The thickness of Co film was 6.1–19.7 nm. The pressure during the evaporation was ~10^{-3} Pa. The deposition rate was 1.5–2.5 nm/min at an evaporation power of 400–450 W. The magnetic field was 380 Oe, which was applied in the in-plane transverse direction of the Co thin films for the induced magnetic anisotropy formation.

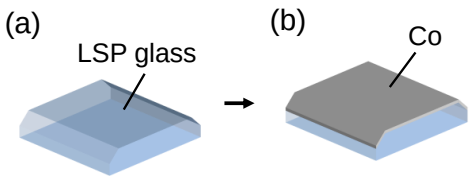

Figure 2.1 Fabrication of Co/glass structure. (a) Chamfered edges formation and (b) Co thin film deposition.

2.2.2 Fabrication of glass/Co/glass structure

Co thin film sandwiched between the LSP glasses was fabricated using a thermal pressing technique. A glass-molding machine (Toshiba Machine Co. Ltd., GMP–00504 V) was used for the pressing. The LSP glass coated with the Co thin film was placed on the sample stage inside the machine. Another LSP glass was stacked on the Co/LSP-glass sample. The stacked sample was heated up to 513°C (10°C higher than the glass deformation temperature) at 2.5°C/s in N_2 atmosphere, kept for 30 s, and then pressed at 0.25 MPa for 5 min (Figure 2.2(a)). After the pressing operation, the pressure was released and cooled down to room temperature at 1°C/s. Subsequently, obtained samples were cut in half (Figure 2.2(b)). The cross-sectional surfaces of LSP-glass/Co/LSP-glass were polished by one-step mechanical polishing (MP) method and two-step chemical mechanical polishing (CMP) method using a polishing machine (Nano Factor Co. LTD., FACT-200) under a rotation speed of 75 rpm at room temperature (Figure 2.2(c)). The MP process was performed on a cast-iron plate (Imahashi MFG. Co., FAC-8IRS) using Al_2O_3-based emeries (FUJIMI INCORPORATED, FO) in the following sequence of particle diameters: 93 (#240), 64 (#400), 46 (#600) and 18 μm (#1200). Thereafter, the first CMP process was performed using a polishing cloth (LAM PLAN, LAM 410) with CeO_2 slurries (Nano Factor Co. LTD.) of a particle diameter of 1 μm in sequence. The second CMP process was performed using a polishing cloth (LAM PLAN, LAM 410) with Al_2O_3 slurries (Baikowski, Baikalox CR30) of a particle diameter of 100 nm.

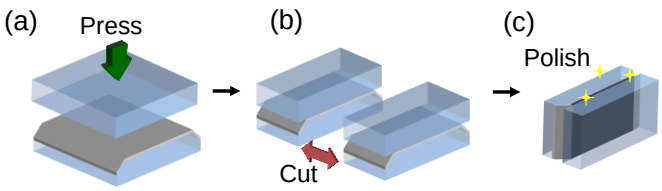

Figure 2.2 Fabrication of glass/Co/glass structure; (a) thermal pressing, (b) cutting, and (c) polishing of stacked glasses cross-section.

2.2.3 Characterization of sample

Co thin film thickness was measured using a Lambert-Beer method, which was performed utilizing a diode pumped solid state (DPSS) laser and a photodiode detector. Morphology and roughness of sample was analysed using an atomic force microscopy (AFM; SII Nano Technology Inc., Nanocute) in air. The polished LSP-glass/Co/LSP-glass cross-sectional microstructure was evaluated using a scanning electron microscopy (SEM; JSM- 6700FT, JEOL) operating at 5 kV. Magnetization curves of Co thin films on LSP glasses were measured using a focused magneto-optical Kerr effect (MOKE; NEOARK, BH-PI920-HU) with a laser spot diameter of 6 μm under a magnetic field between −1 kOe and +1 kOe at room temperature. Magnetization curves of the samples were also measured using a magnetic property measurement system (MPMS; Quantum Design, Inc.) under between −10 kOe and +10 kOe at room temperature. Stray field generating from the Co thin film edges were observed using a magnetic force microscopy (MFM; SII Nano Technology Inc., Nanocute), in which a CoCrPt-coated cantilever was used.

The local magnetic fields generated between the edges of two Co thin-film electrodes in SQC devices were calculated using a micromagnetic simulation. The calculation region has semi-infinite space corresponding to SQC devices. The region was divided into 0.1 nm×0.1 nm×0.1 nm cubic mesh. The stray field computation was carried out using demagnetization tensor and numerical integration. Fortunately, the demagnetization coefficient of SQC was approximately zero. Since the magnetization in SQC almost orients to the *x*-direction, the stray field was obtained from the most contribution due to magnetic charges at the SQC edges.

2.3 Results and Discussion

2.3.1 Co thin film on LSP glass

2.3.1.1 Surface roughness of LSP glass and Co thin film on LSP glass

Figure 2.3 shows the schematic view of SQC device. Nanoscale junction is obtained by crossing two film edges. Therefore, the junction area is determined by the multiplication of two film thicknesses. Such small junction area is influenced by the film surface roughness. Therefore, I investigated the surface roughnesses of bare LSP glass and the Co thin films on LSP glasses. Figure 2.4(a) shows the root mean square surface roughness (R_q) as a function of the Co thin film thickness on LSP glasses. For comparison, the surface roughness of Co thin films on PENs is also shown. The PEN and Co/PEN samples were examined as a magnetic thin-film electrode of SQC device in our previous study [7]. Insets show AFM surface images of LSP glass and Co/LSP-glass. Scanning area is 500×500 nm^2. Here, R_q is defined by $R_q = \sqrt{1/L_x L_y \int_0^{L_x} \int_0^{L_y} |h\,(x,y)|^2 dxdy}$, where $h\,(x, y)$ is the height profile as a function of x and y, and $L_{x(y)}$ is the scanning size along the x (y) direction. The surface roughness of Co on LSP glass is as small as 0.87–1.20 nm. From Figure 2.4(a), the R_q value is 1.23–1.50 nm, which is smaller than that of Co thin film on PEN. Such smoothness is attributed not only to the LSP glass surface but also a low deposition rate of Co thin films. The vaporized Co atoms can move easily and freely along the in-plane direction on LSP glass surface. The low deposition rate of 0.15 nm/s provides an adequate time to the Co atoms to diffuse on the surface. Such Co atom diffusion contributes the formation of smooth surface with low surface energy. Figure 2.4(b) shows the scaling properties of the R_q for the bare LSP glass and Co thin films on LSP glasses. As shown in Figure 2.4(b), the R_q of Co thin films (t = 9–21 nm) on the LSP glasses are as small as 0.06–0.30 nm at the same scanning scale as their film thicknesses, which are corresponding to less than a few atomic layers. These results indicate that the R_q of the Co film on LSP glass has little or no influence on the nanoscale junction area in the SQC device.

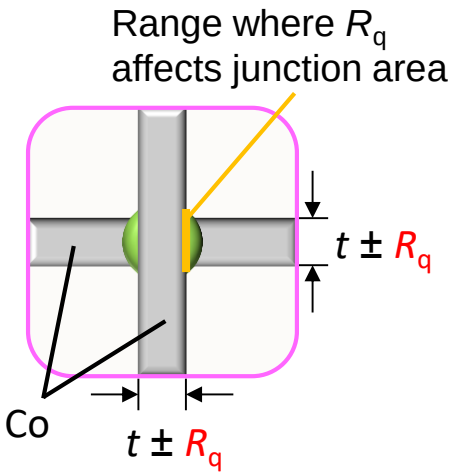

Figure 2.3 Schematic image of junction area.

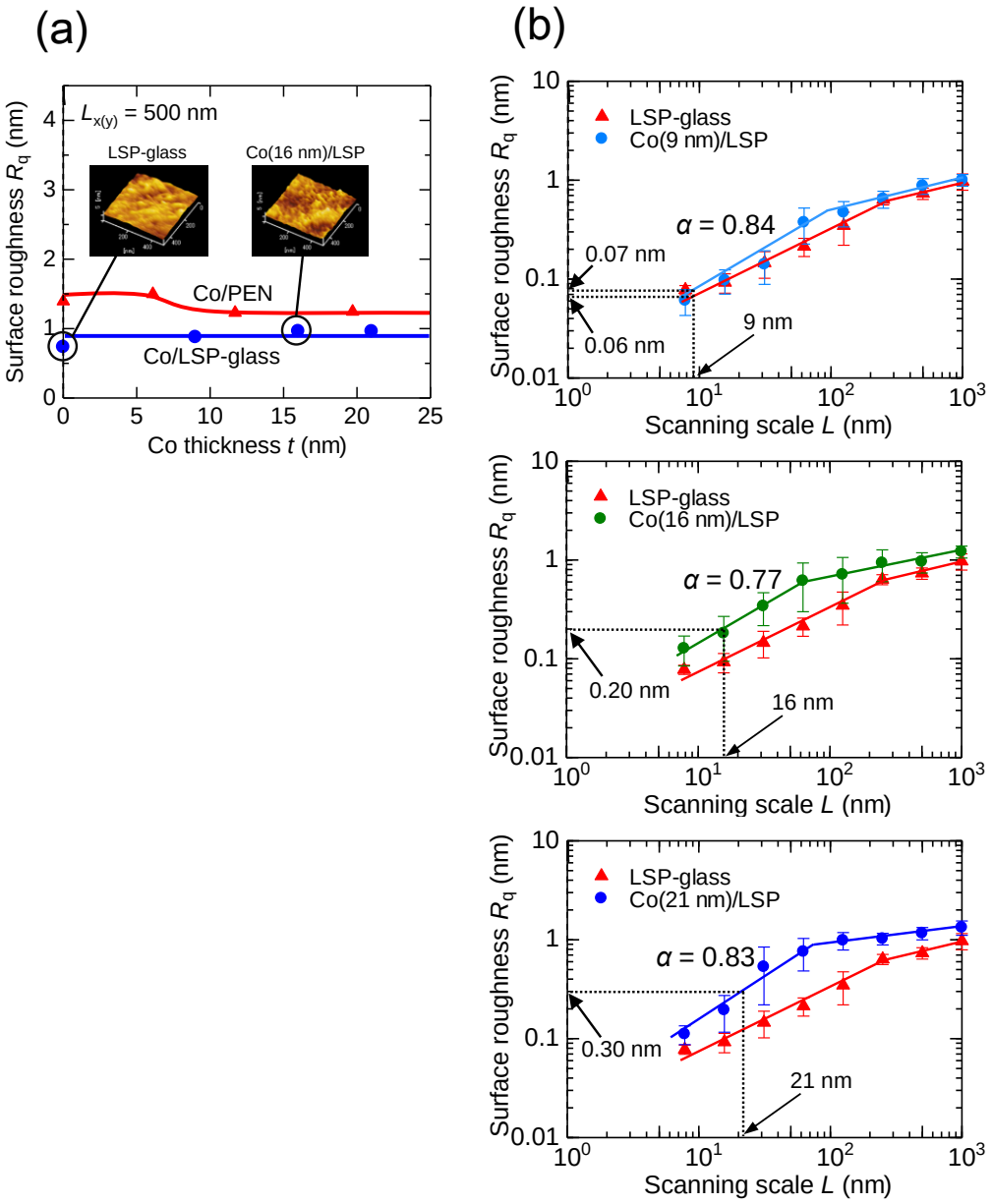

Figure 2.4 (a) Surface roughness as function of Co thickness in Co/LSP-glass and Co/PEN, (b) scaling properties of the surface roughness for LSP glass, Co(9 nm)/LSP, Co(16 nm)/LSP and Co(21 nm)/LSP.

2.3.1.2 Growth mode of Co thin film on LSP glass

In this section, the growth mode of Co films on LSP glasses is discussed from the scaling properties of surface roughness (R_q). The surface roughness shown in Figure 2.4 (b) follows a scaling law, $R_q = w(L) \propto L^{\alpha}$, where $w(L)$ is the interface width, which corresponds to the standard deviation of surface height; L is the system size and α is the growth scaling exponent. The values of α remain almost constant at 0.77−0.84 for the Co thin films on LSP glasses, as indicated by the similar roughness slope for each sample. This means that the surface morphologies of Co thin films on LSP glasses are independent of the film thickness. I also note that the surface can be described by a self-affine structure due to $\alpha \neq \beta$, where β is the dynamical exponent in the scaling law $R_q = w(t) \propto t^{\beta}$. Here, t is the film thickness. As can be seen in Figure 2.4(a), the dynamical exponent β of Co thin films on LSP glasses is nearly equal to zero because R_q is almost the same at each Co thickness. This results in $\alpha \neq \beta$, indicating a self-affine growth regime, which can also be observed in Cu films deposited on glasses [8].

2.3.1.3 Magnetic property of Co thin film on LSP glass

Figure 2.5(a) shows the magnetization curves of Co thin films on LSP glasses obtained by the MOKE measurements. The film thicknesses are 8.5, 11, 15.9, and 17.5 nm, respectively. Magnetic field was applied in the magnetic easy-axis direction during the measurement. The coercivities of a Co thin films on LSP glasses is 20–30 Oe, which is almost the same as the values reported for Co films on Si(001) wafer [9]. On the other hand, the magnetization curve of the Co(21 nm)/LSP-glass sample was measured using MPMS. The result is shown in Figure 2.5(b). The influence of LSP glasses as the diamagnetic material was eliminated in advance. As shown in Figure 2.5(b), the shape of the magnetization curve with coercivity of 25 Oe was almost the same as the results obtained by the MOKE technique (Figure 2.5(a)). The magnetization M of Co thin films can

be calculated as $M = m/V$, where V is the Co thin film's volume and m is the saturation magnetic moment obtained from MPMS measurement. Using this equation, the magnetization M is calculated to be 830 emu/cc, when V = 21 nm×4.03 mm×8.00 mm and m = 0.000562 emu. The magnetization is low compared to that of a bulk Co (M = 1424 emu/cc) [10]. It is thought that the magnetism of the Co film is lost to several nanometers from the interface with LSP glass [11].

Next, I discuss the squareness of the hysteresis loop of Co thin film deposited on LSP glass and PEN. The squareness of the hysteresis loop is defined with M_r/M_s, where M_r and M_s are remanent and saturation magnetization, respectively. The squareness as a function of Co thin film thickness is shown in Figure 2.6. The squareness of the hysteresis loop of Co thin films on LSP glasses is as large as 0.96–1.0, which is greater than that of Co thin films on PEN of 0.32–0.84. This large squareness causes a high stray field to be generated from the edges of Co thin-film electrodes in SQC devices.

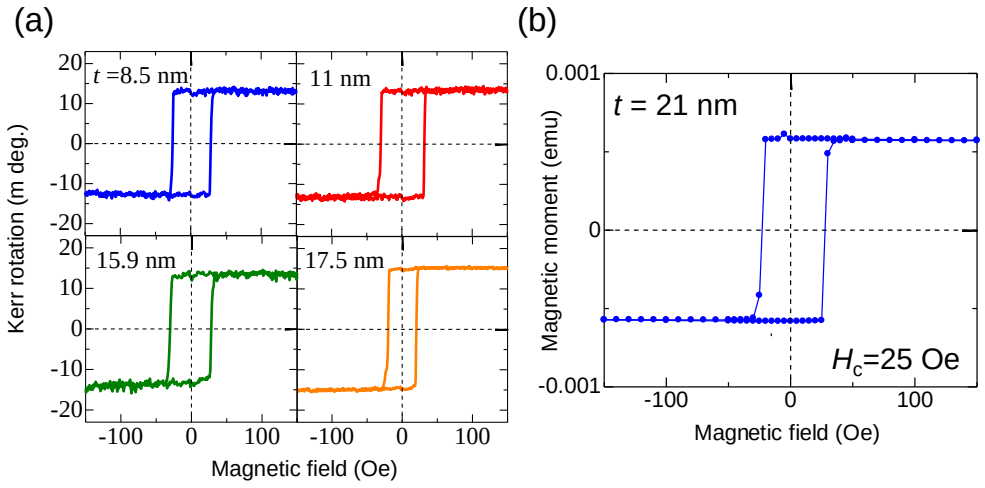

Figure 2.5 Magnetization curves of Co thin films on LSP glasses measured using (a) MOKE and (b) MPMS.

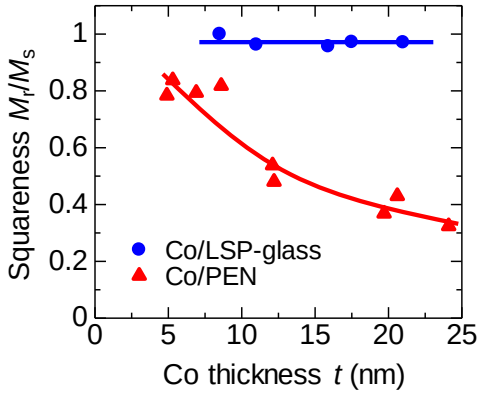

Figure 2.6 M_r/M_s values as function of Co thicknesses in deposited on LSP glasses and PENs, respectively.

Next, I discuss the magnetic domain structure of Co film deposited on LSP glass. Figure 2.7(a) shows the magnetization curves for Co film (t = 21 nm) using the MOKE technique. These curves were obtained in the external magnetic field applied at an angle of 2, 42 and 79 degrees from the magnetic easy-axis direction. The coercivity of magnetization curves gradually decreased with increasing the angle between the magnetic-field and the easy-axis directions. The coercivity was minimized when the magnetic field is applied in the hard-axis direction. These results indicate that a magnetic anisotropy was induced in the Co thin films. Figure 2.7(b) shows the Co film coercivities as a function of the angles between the magnetic-field and the easy-axis directions. The coercivity at each angle was normalized using the value at θ = 42°. The experimental values were consistent with the calculated result using Stoner-Wohlfarth model which can be applied to single magnetic domain structure. Therefore, the Co films on LSP glasses were thought to have single domain structure.

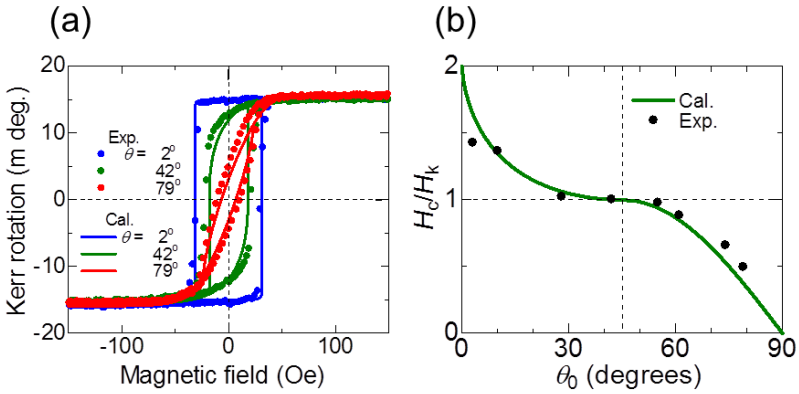

Figure 2.7 (a) Magnetization curves of Co thin film on LSP glass measured using MOKE. The magnetic field is applied at angle of 2, 42 and 79 degrees taking from magnetic easy-axis direction. (b) Coercivities of Co thin film on LSP glass as function of measuring angle, and calculation value by Stoner-Wohlfarth model.

2.3.2 Co thin film sandwiched between LSP glasses

2.3.2.1 Polished cross-sectional surface of glass/Co/glass

After the thermal pressing process, highly smooth LSP-glass/Co/LSP-glass cross-sectional surface is obtained using the MP and CMP methods. The MP process is performed using Al_2O_3-based emeries with different particle diameters: 93, 64, 46, 18, and 13 μm. Next, the cross-sectional surface was polished using the first CMP process with CeO_2 slurries of a particle diameter of 1 μm, and then with Al_2O_3 slurries of a particle diameter of 0.1 μm. Figure 2.8 shows the polished surfaces roughnesses of Co thin-film edges sandwiched between LSP glasses as a function of the particle diameters d_{MP} (the MP process) and d_{CMP} (the CMP process). It is evident that the surface roughness decreases depending on the d_{MP} and d_{CMP}.

Figure 2.9(a) shows the SEM image of the polished cross-sectional surface of LSP-glass/Co/LSP-glass. The Co thin film thickness is 14 nm. Clear edge was confirmed in the SEM photograph. The contrast enhancement of the edge is attributed to the high conductivity of Co. Figure 2.9(b) shows the AFM view in the vicinity of Co edge. The polished surfaces roughness is as small as 0.29–1.2 nm in a scanning area of 1×1–30×30 μm^2.

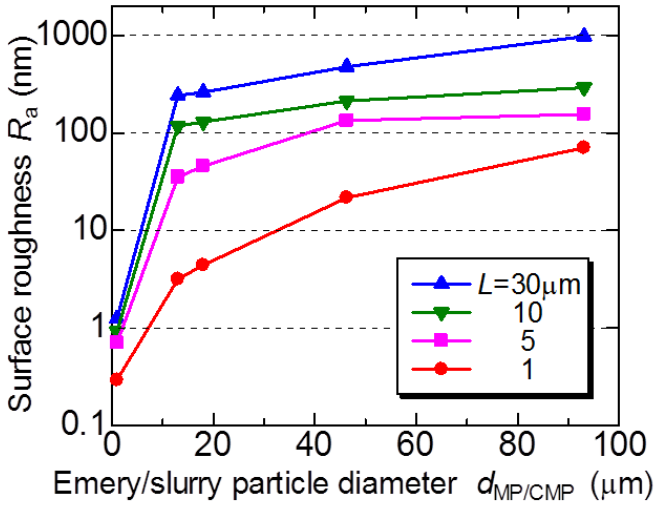

Figure 2.8 Surface roughness of polished LSP-glass/Co/LSP-glass observed using the AFM as function of diameter $d_{MP/CMP}$ of Al_2O_3-based emeries (d_{MP} > 10 μm) or CeO_2 slurries (d_{CMP} = 1 μm).

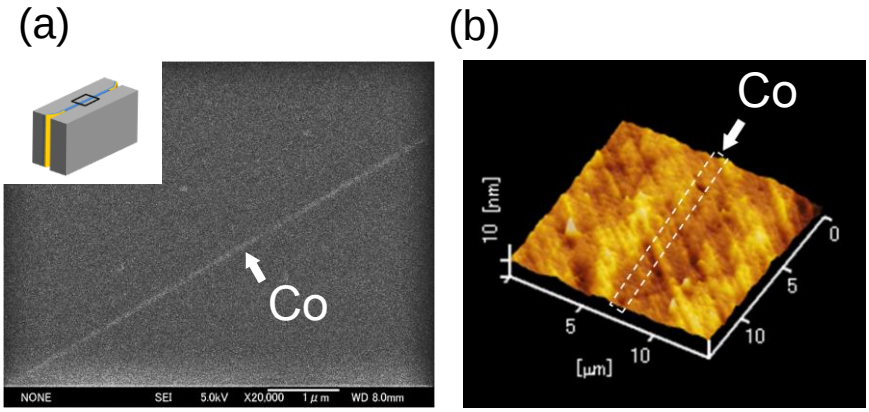

Figure 2.9 Polished cross-sectional surface of LSP-glass/Co/LSP-glass images; (a) SEM and (b) AFM.

The flat LSP-glass/Co/LSP-glass cross-sectional surface enables the MFM measurement of stray field from the Co edge. Figure 2.10 shows MFM images of the polished surfaces of Co thin film sandwiched between LSP glasses. The Co thin films thicknesses are 8.5, 11, and 15 nm, respectively. Blue colored bars in the MFM images indicate that the stray field is generated along the out-of-plane direction of the samples. As can be seen from Figure 2.10, a strong stray field is generated along the out-of-plane direction from the Co edges. This behavior is consistent with the results obtained by the MOKE measurements, indicating that the squareness of the hysteresis loop is as large as 0.96–1.0, as shown in Figure 2.6. Here, I note that the stray field width is about 0.5–1 μm, which is much larger than the Co thickness. This is attributed to a long spacing distance (~50 nm) between the Co thin-film edge and the CoCrPt-coated cantilever probe of the MFM setup. The distance prevents the magnetization reversal of the CoCrPt-coated cantilever probe.

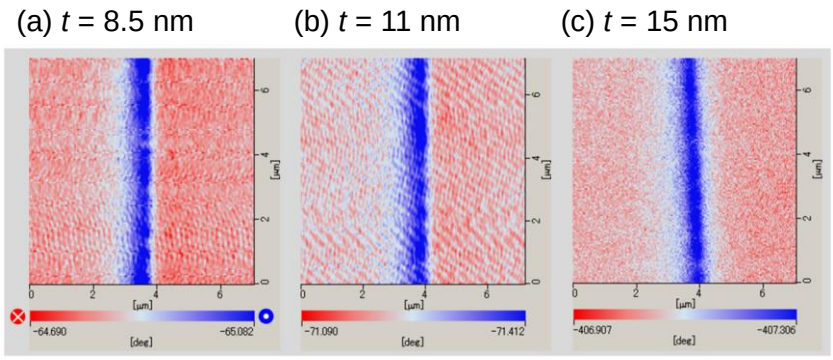

Figure 2.10 MFM images of polished LSP-glass/Co/LSP-glass surfaces; Co thicknesses are (a) 8.5, (b) 11, and (c) 15 nm, respectively.

2.3.2.2 Calculation of stray magnetic field between crossed edges of two Co thin films

I successfully established the fabrication method of ultra-flat LSP-glass/Co/LSP-glass cross-sectional surface. If two Co thin film edges are crossed with an adequate distance, an SQC device will be fabricated. Then, in this section, the stray magnetic field generated between the crossed edges of two Co thin-film electrodes in the SQC device (Figure 2.11(a)) is calculated. The calculated results are shown in Figure 2.11(b). The insets show the distribution of the stray field for varying Co thicknesses t and distances between the two edges of Co thin-film electrodes d; specifically, t = 5 nm, d = 20 nm; t = 5 nm, d = 5 nm; and t = 20 nm, d = 5 nm. The points x and y are the positions along the in-plane and out-of-plane directions of the Co films, respectively, between the two edges of Co thin-film electrodes. The position $x = y = 0$ nm is the center of the junction between the two edges of Co thin-film electrodes. At t = 5 nm and d = 20 nm, the stray field is less than 2 kOe, and a uniform distribution is not obtained. At t = 5 nm and d = 5 nm, although the stray field is beyond 4 kOe, a uniform distribution is still not obtained. At t = 20 nm and d = 5 nm, the stray field measures as high as 7 kOe, and a uniform distribution is successfully obtained. From the calculation plots of Figure 2.11(b), it is found that a high stray field beyond 6 kOe is generated when the Co thickness is larger than 10 nm and the distance between the two edges of Co thin-film electrodes is 5 nm. This high magnetic field produces a large Zeeman effect in the sandwiched materials between the two edges of magnetic thin-film electrodes. These experimental and calculation results conclude that SQC devices with Co thin-film electrodes sandwiched between LSP glasses (Co thickness t = 10–20 nm) can be used as spin-filter devices.

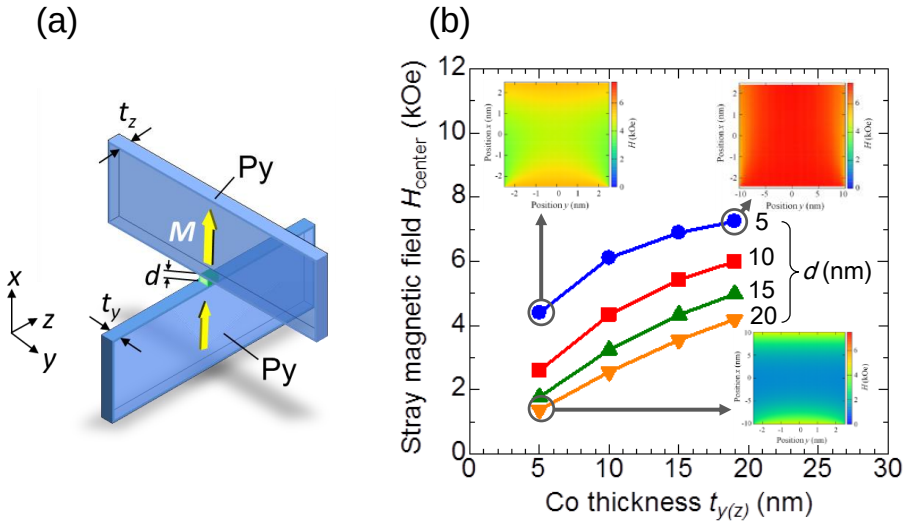

Figure 2.11 (a) Structure of an SQC device for calculation of stray field and (b) calculation results of Co thickness dependence of stray magnetic field between two edges of Co thin-film electrodes in SQC devices. The insets show stray field distribution; t = 5 nm and d = 20 nm, t = 5 nm and d = 5 nm, and t = 20 nm and d = 5 nm, respectively.

2.4 Conclusion

In this chapter, I demonstrated the formation of Co thin films on LSP glasses and between LSP glasses. Their morphologies and magnetic properties were investigated in detail. The surface roughness of a Co thin film (t = 21 nm) on an LSP glass is less than 0.30 nm at the same scanning scale as the Co film thickness. The smooth Co thin films were attributed not only to the use of LSP glasses with a smooth surface but also a low deposition rate of Co thin films. The magnetization curves of Co thin films ($t \leq 21$ nm) deposited on LSP glasses showed the coercivity of 20–30 Oe. Furthermore, the squareness of their hysteresis loop was shown to be as large as 0.96–1.0. Next, characteristics of Co thin-film electrodes sandwiched between the LSP glasses were investigated. As a result of the establishment of polishing techniques for Co thin-film electrodes, the formation of smooth LSP-glass/Co/LSP-glass cross-sectional surface was successfully demonstrated.

Subsequently, the generation of stray magnetic fields from the Co edge was confirmed by the MFM measurement. Theoretical calculation exhibited that a high stray field beyond 6 kOe is generated between the two edges of Co thin-film electrodes when the Co thickness is larger than 10 nm at a junction gap distance of 5 nm. These results indicate that the Co thin films on LSP glasses are good candidates for the magnetic thin-film electrodes in SQC devices.

2.5 Reference

1. C. A. F. Vaz and J. A. C. Blanda, *J. Appl. Phys.* **89** (2001) 7374.
2. B. Presa, R. Matarranz, C. Clavero, J. M. García-Martín, J. F. Calleja and M. C. Contreras, *J. Appl. Phys.* **102** (2007) 053901.
3. B. N. Engel, M. H. Wiedmann, R. A. Van Leeuwen and C. M. Falco, *J. Appl. Phys.* **73** (1993) 6192.
4. A. Kharmouche, S. M. Chérif, A. Bourzami, A. Layadi and G. Schmerber, *J. Phys. D: Appl. Phys.* **37** (2004) 2583.
5. J. S. Suen, M. H. Lee, G. Teeter, and J. L. Erskine, *Phys. Rev. B* **59** (1999) 4249.
6. J.W.C. De Vries, *Thin Solid Films* **167** (1988) 25.
7. H. Kaiju, T. Abe, K. Kondo, and A. Ishibashi, *J. Appl. Phys.* **111** (2012) 07C104.
8. K. Ohkawa, T. Nakano, S. Baba, *J. Vac. Soc. Jpn.* **45** (2002) 134.
9. S. P. Li, A. Lebib, D. Peyrade, M. Natali, and Y. Chen, *Appl. Phys. Lett.* **77** (2000) 2743.
10. P. H. Dederichs, R. Zeller, H. Akai, and H. Ebert, *J. Magn. Magn. Mater.* **100** (1991) 241.
11. K. Kondo, H. Kaiju, and Akira Ishibashi, *Jpn. J. Appl. Phys.* **52** (2013) 013001.

Chapter 3

Structural and magnetic properties of $Ni_{78}Fe_{22}$ thin films sandwiched between glasses and their application in spin-filter devices

---

3.1 Introduction

In chapter 2, I successfully demonstrated the formation of smooth LSP-glass/Co/LSP-glass cross-sectional surfaces using the thermal pressing technique and polishing methods. Furthermore, the generation of the stray magnetic fields from the Co edge was confirmed. These results promise that the LSP-glass/Co/LSP-glass structure can be used for the electrodes of SQC devices. Other ferromagnetic materials, such as Fe and Ni, will also be used for the electrode. Particularly, NiFe alloy is an excellent electrode material for spintronic devices or magnetic soft/hard materials due to its large magnetization, high controllability of spin transports, and long-term stability in air [1−5]. In this chapter, I investigate the properties of $Ni_{78}Fe_{22}$ (parmalloy, Py in the following) thin films on the LSP glasses and the films sandwiched between LSP glasses. I also reveal the influence of the thermal pressing process on the properties of the Py thin films sandwiched between LSP glasses. Moreover, the stray magnetic field generated between crossed edges of two Py thin films in SQC devices is calculated using a micromagnetic simulation. Finally, the applicability of SQC structures to spin-filter devices is discussed.

3.2 Experimental

3.2.1 Fabrication of Py thin film on glass substrate

As shown in Figure 3.1(a), The LSP glass substrates with dimensions of $10\times10\times2$ mm^3 were prepared and chamfered on both sides. The LSP glasses were cleaned in an ultrasonic bath with acetone and ethanol for 10 min, respectively. Afterwards, Py thin films with thicknesses of 10–100 nm were deposited on the LSP glasses using an ion-beam sputtering method under an in-plane magnetic field of 400 Oe. (Figure 3.1(b)). The base pressure before sputtering was $1.0–5.0\times10^{-5}$ Pa. The deposition rate of Py thin films was 3 nm/min at a sputtering power of 60 W (1.0 kV and 60 mA) under an Ar pressure of $3.0−4.5\times10^{-2}$ Pa.

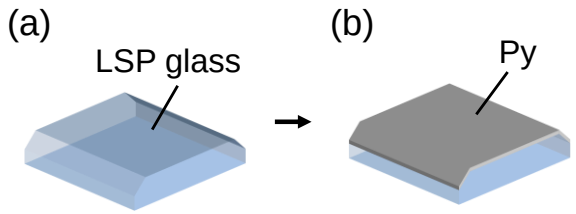

Figure 3.1 Fabrication of Py/LSP glass structure: (a) chamfered edges formation and (b) Py thin film deposition.

3.2.2 Fabrication of glass/Py/glass structure

To reveal the influence of pressure in thermal pressing process, Py thin films sandwiched between the LSP glasses was fabricated using a thermal pressing machine (Toshiba Machine Co. Ltd., GMP–00504V) at a pressure of 0.25–1.0 MPa. Other thermal pressing conditions were same as described in chapter 2.

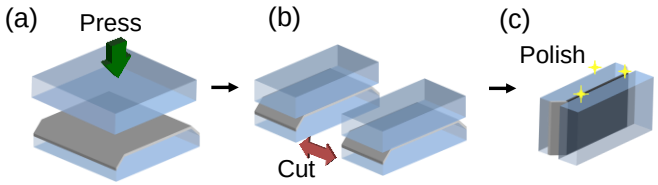

Figure 3.2 Fabrication of glass/Py/glass structure; (a) thermal pressing of two glasses, (b) cutting, and (c) polishing of stacked glass cross-section.

After the pressing operation, the pressure was released and cooled down to room temperature at 1°C/s. Subsequently, obtained samples were cut in half (Figure 3.2(b)). The cross-sectional surfaces of LSP-glass/Py/LSP-glass were polished using following two methods; one-step mechanical polishing (MP) method and two-step chemical mechanical polishing (CMP) method (Figure 3.2(c)). The MP process was performed in the same manner as described in chapter 2. Thereafter, the first CMP process was performed using a polishing cloth (Struers, DP-DUR) with diamond pastes (Struers, DP-paste) of a particle diameter of 3 and 1 μm in sequence. The second CMP process was performed using a polishing cloth (Struers, DP-Chem) with colloidal SiO_2 slurries (Struers, OP-S) of a particle diameter of 40 nm. These CMP processes were carried out using a polishing machine (Nano Factor Co. LTD., FACT-200) under a rotation speed of 75 rpm at room temperature.

3.2.3 Characterization of sample

The cross-sectional microstructure and interfacial features of the samples were examined using a transmission electron microscopy (TEM; JEOL, JEM−ARM200F), a transmission electron diffraction (TED), and a TEM–energy dispersive X-ray spectroscopy (EDS) operating at 200 kV. TED patterns of the samples were obtained with a beam size of 100 nm. TEM specimens were prepared by a focused ion beam (FIB; Hitachi High-Tech. Corp., FB-2100) system. The thickness of Py thin films was estimated both by a TEM observation and a Lambert-Beer method using a diode-pumped solid-state (DPSS) laser and a photodiode detector. Py thin film thickness was also

measured using a stylus surface profiler (Kosaka Laboratory Ltd., ET200).

Average crystal grain size in Py thin films was determined using an X-ray diffraction (XRD; Rigaku, SmartLab). The magnetization curves of Py thin films on LSP glasses and Py thin films sandwiched between LSP glasses were measured using a MOKE and/or MPMS. The surface morphology and roughness of the sample were analysed using an AFM in air. The stray field originating from the edge of Py thin film was measured using an MFM. A stray field generating from the Py thin film edge was observed using the MFM, in which a CoCrPt-coated cantilever was used.

The local magnetic fields generated between the two edges of Py thin-film electrodes in SQC devices were calculated using a micromagnetic simulation. (Refer to chapter 2.2.3 for the calculation technique.)

3.3 Results and Discussion

3.3.1 Py thin film on LSP glass

3.3.1.1 Cross-sectional structure of Py thin film on LSP glass

Figure 3.3 shows the cross-sectional bright-field TEM images of Py thin films with a thickness of 17 nm and 86 nm deposited on LSP glasses, which are denoted by Py17 and Py86, respectively (integer numbers are the Py layer thicknesses in nm). Carbon layers were deposited on the Py thin films for protection. There was no diffusion of Ni and Fe atoms into the LSP glass, resulting in the clear interface between Py thin films and LSP glasses.

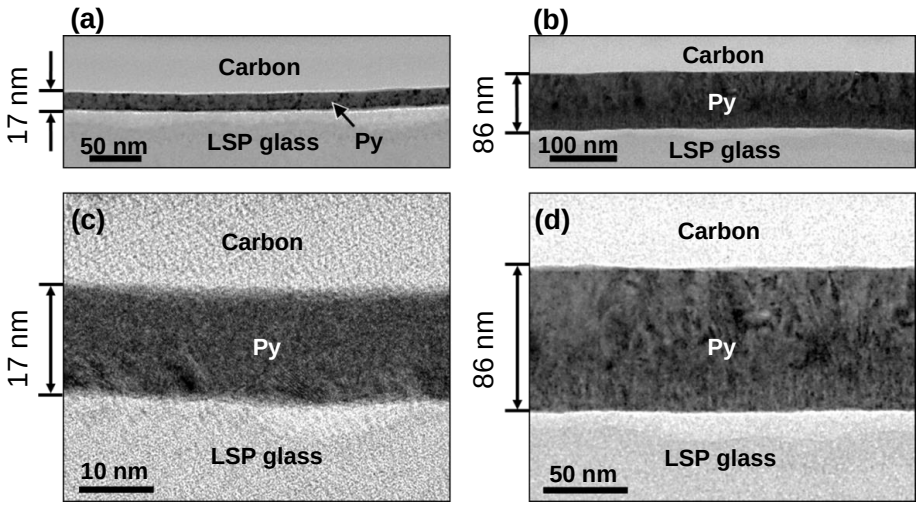

Figure 3.3 Cross-sectional TEM images of (a) Py17 and (b) Py86. (c) and (d) are high-resolution images of (a) and (b), respectively.

The clear interface was also confirmed by the cross-sectional TEM-EDS mapping images of Py86 as shown in Figure 3.4. Some researchers have pointed out that metal atoms diffuse into the materials, which have a low softening point, in the process of deposition. [6,7]. For example, a cross-sectional TEM observation of the interface between Au and polymethyl methacrylate (PMMA) prepared by a dip-coating demonstrated that the thickness of interfacial region ranges from 2 to 4 nm, which suggests the Au atom diffusion into PMMA layer [6]. In another study, radio-tracer measurements in conjunction with an ion-beam depth profiling of Ag/trimethylcyclohexane polycarbonate (TMC-PC) revealed that the traces of Ag atoms can be detected at 400 nm depth from the TMC-PC surface [7]. In contrast, such diffusion did not occur at the Py/LSP-glass interface. This result means that Py thin films on B_2O_3-based LSP glasses are good candidates for electrodes of SQC devices.

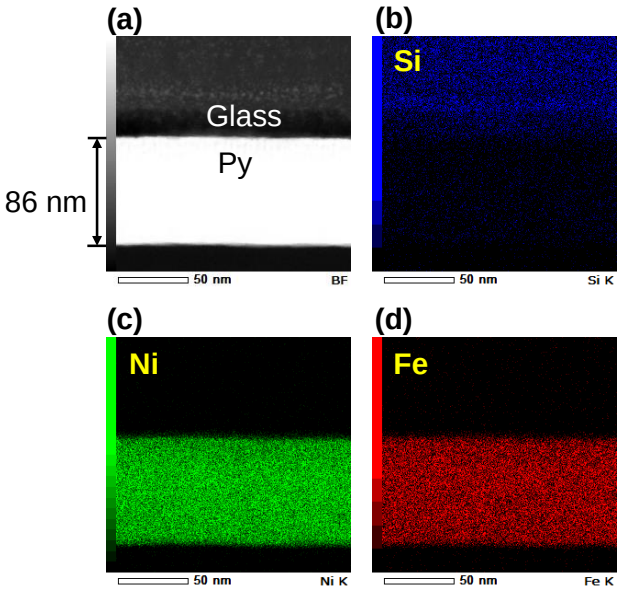

Figure 3.4 (a) Cross-sectional TEM image of Py 86, and EDS mapping images for (b) Si, (c) Ni, and (d) Fe, respectively.

3.3.1.2 Surface roughness and growth mode of Py thin film on LSP glass

Figure 3.5 shows the dependence of the surface roughness R_q on the thickness of Py thin films on LSP glass. The definition of surface roughness R_q was described in chapter 2. The R_q values of Py thin film on PEN, which have been already examined as the magnetic thin-film electrodes of SQC devices [8], are also plotted. The insets show the surface AFM images of an LSP glass, Py17, and Py86, respectively. The scanning area was 500×500 nm^2. The R_q values were investigated in randomly selected 10 areas at each Py with different thickness. The average value in these areas is plotted in Figure 3.5. As can be seen in this figure, the R_q values of Py thin films on LSP glasses (0.73−0.88 nm) are smaller than those of Py thin films on PEN (1.65−1.68 nm). The R_q values are also almost similar to or slightly smaller than those of Co/LSP-glass (0.87−1.2 nm) [9]. The smooth surfaces of the Py thin films on LSP glasses are consistent with the TEM results shown in Figure 3.3.

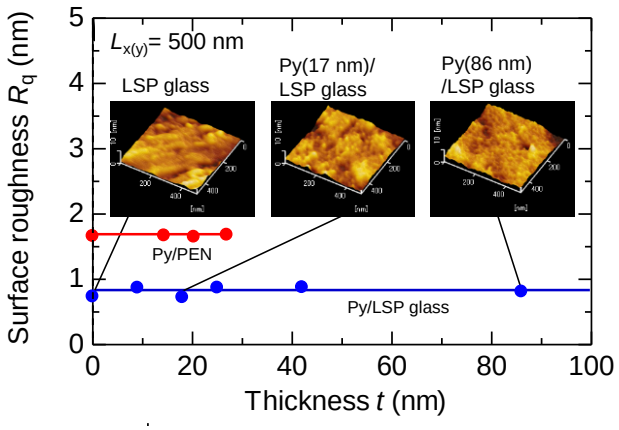

Figure 3.5 Surface roughness as a function of film thickness for Py thin films on LSP glasses.

Figure 3.6 shows the scaling properties of surface roughness R_q for an LSP glass and Py thin film on LSP glass. As described in chapter 2, The R_q obeys a scaling law, $R_q = w(L) \propto L^{\alpha}$, where $w(L)$ is the interface width, which corresponds to the standard deviation of the surface height; L is the system size; and α is the growth scaling exponent. The α values remain almost constant between $0.59-0.61$ for LSP glass and Py thin films on LSP glasses. As shown in Figure 3.5, the dynamical exponent β of Py thin films on LSP glasses in the scaling law $R_q = w(t) \propto t^{\beta}$ is nearly equal to zero. Here, t is the film thickness. These scaling laws result in $\alpha \neq \beta$, indicating a self-affine growth regime which can also be observed in the deposited Py thin films on PEN substrates [8].

Here, I discuss the application of Py thin films to SQC devices from the viewpoint of surface roughness. As described in chapter 2, the junction area of an SQC device is determined by the film thickness. Therefore, the surface roughness must be sufficiently small at a scanning scale equal to the film thickness. As shown in Figure 3.6, the R_q of the Py9 and the LSP glass are as small as 0.11 and 0.07 nm at a scanning scale of 9 nm, respectively, corresponding to a few atomic layers. The surface roughness of Py86 is less than 0.5 nm at a scanning scale equal to the Py thickness. These results indicate that Py thin films on LSP glasses are useful as electrodes for SQC devices from the perspective of surface morphologies as well as interfacial structures.

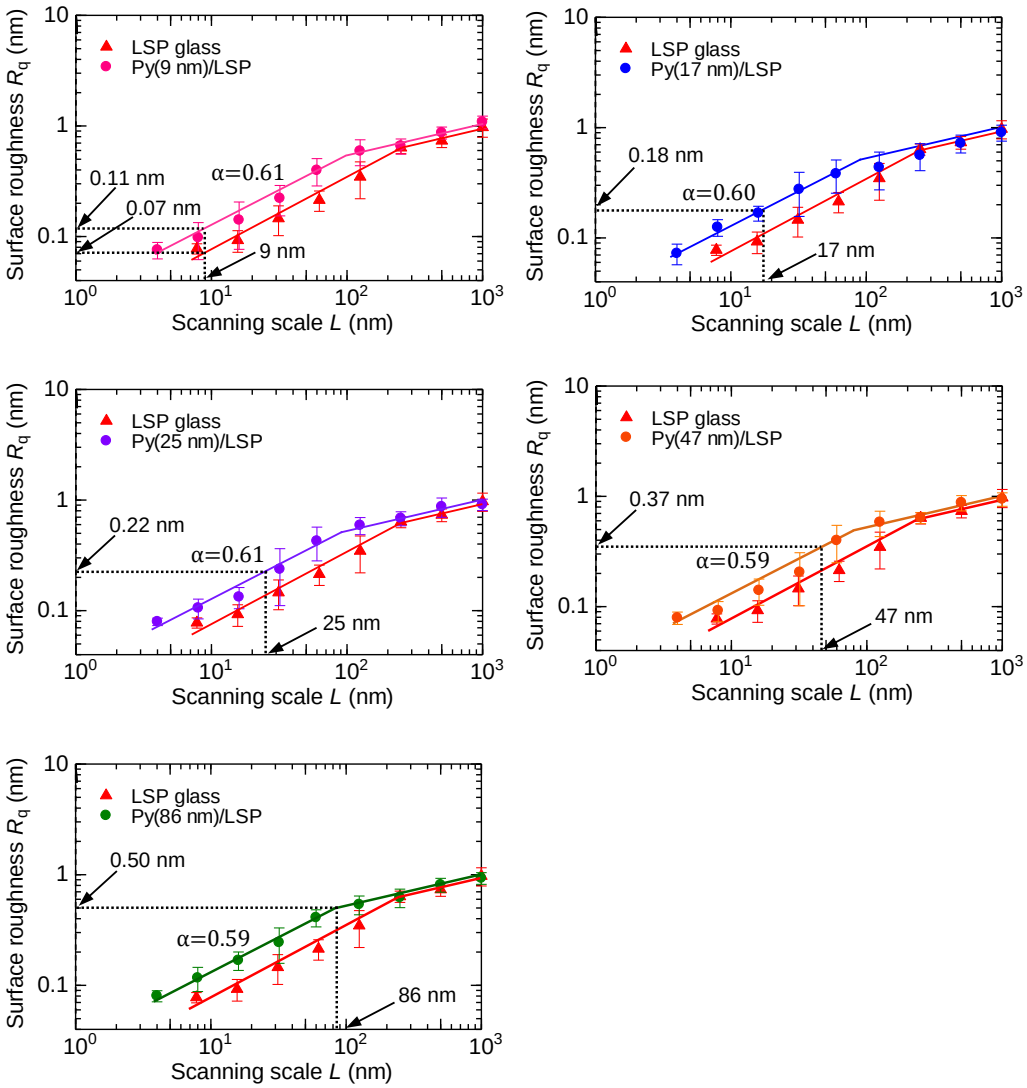

Figure 3.6 Scaling properties of surface roughness for LSP glass, Py9, Py17, Py25, Py47, and Py86.

3.3.1.3 Magnetic property of Py thin film on LSP glass

Figure 3.7 shows the magnetization curves for Py17 and Py86 measured using a MOKE technique. The magnetic field was applied in the *x* and *z* directions, as shown in the inset of Figure 3.7(a), which correspond to the directions of magnetic easy-axis and hard-axis, respectively. The magnetic anisotropy was induced in both of the Py thin films, which were similar to the magnetic properties of Co thin films shown in chapter 2. The coercivity of Py17 was as low as 0.9 Oe (Figure 3.7(a)), which is almost the same as the typical value for Py films [5]. The squareness of the hysteresis loop M_r/M_s was as large as 0.99. Here, M_r and M_s are the remanent and saturation magnetizations, respectively. The similar magnetic behavior was observed in Py86, in which the coercivity was 1.1 Oe and the squareness was 0.98, respectively.

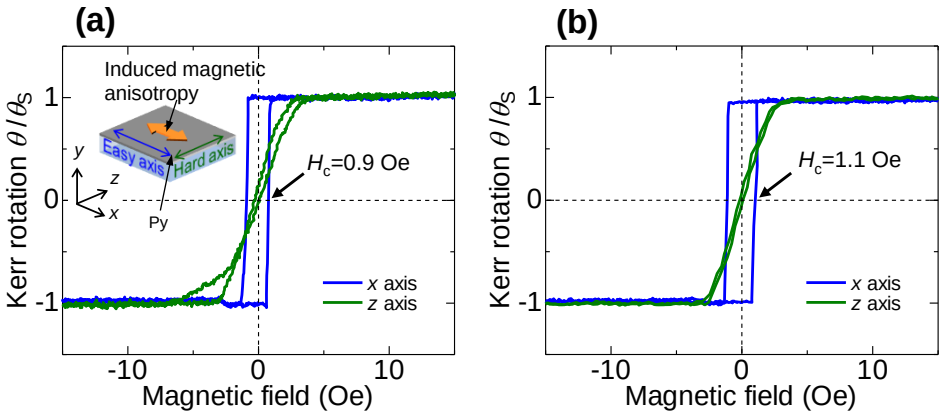

Figure 3.7 Magnetization curves of (a) Py17 and (b) Py86 measured using MOKE technique.

3.3.2 $Ni_{78}Fe_{22}$ thin film sandwiched between LSP glasses

3.3.2.1 Cross sectional observation of Py thin film

Figure 3.8(a) and (b) show the cross-sectional TEM images of two kinds of Py thin films sandwiched between LSP glasses after thermal pressing at 1.0 MPa. The thicknesses of the Py thin films before thermal pressing were 17 and 86 nm, respectively. These specimens are denoted as s-Py17 and s-Py86, respectively, in the following. The TEM images indicated that the thicknesses of Py layer decreased to 13 nm for the s-Py17 and 78 nm for the s-Py86, respectively, after thermal

pressing. It is evident that the smooth and clear interface was formed for both the s-Py17 and the s-Py86. There was no diffusion of Fe and Ni atoms into the LSP glasses. The formation of nanolines and flat edge surfaces is an indispensable requirement for leading to the creation of nanoscale junctions in SQC devices. Next, I focus on the thickness change of the Py thin films after thermal pressing. The volume of Py film in the s-Py17 was changed from 8.28 mm×9.99 mm×17 nm to 8.64 mm×11.05 mm×13 nm after the thermal pressing. This corresponds to a 12% decrease in volume. On the other hand, the volume of Py film in the s-Py86 changed from 8.38 mm×10.18 mm×86 nm to 8.54 mm×10.98 mm×78 nm, corresponding to a 0.3% decrease in volume. These results indicate that the volume change of thinner films is more likely to be affected by the thermal pressing than that of thick films. These volume changes are attributed to the crystallinity in Py films.

Figure 3.8(c) and (d) show the high-resolution cross-sectional TEM images of the s-Py17 and the s-Py86, respectively. In comparison with Figure 3.3(c) and (d), it is apparent that the crystal grain size in the Py films increased after the thermal pressing process. The s-Py17 exhibited a highly oriented crystalline structure. On the other hand, a polycrystalline structure with a grain size of ~10 nm was observed in the s-Py86. The increase of the grain size means the reduction of the grain boundary area, contributing to the decrease in volume. I also note that the films elongate in the direction perpendicular to the pressing axis. The elongation of the films is considered to give an influence on the interfacial region; the shear can be applied to the Py films near the Py/LSP interfacial region by elongating the Py film. Such shear stress gives an influence on the crystal growth of Py near the interfacial region. This is consistent with the result that there was a significant volume change for thinner samples.

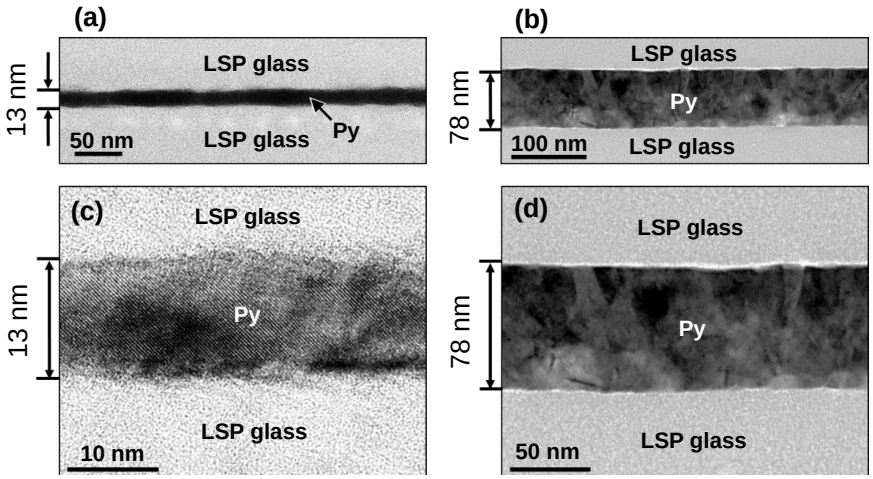

Figure 3.8 Cross-sectional TEM images of (a) s-Py17 and (b) s-Py86 under thermal pressing at *P* = 1.0 MPa. High-resolution cross-sectional TEM images of (c) s-Py17 and (d) s-Py86, respectively.

3.3.2.2 Magnetic property of Py thin film sandwiched between LSP glasses

Figures 3.9(a) and (b) show the magnetization curves of the s-Py17 and the s-Py86 measured using a MOKE technique. These are the same specimens shown in Figure 3.8. The magnetic field was applied in the *x* and *z* directions, as shown in the inset of Figure 3.9(a). The magnetization curves of thermal pressing samples drastically changed compared to those of Py films before thermal pressing (Figure 3.7). The magnetic anisotropy vanished, and the coercivity increased in the thermal pressing samples. In paticular, the coercivity was enhanced from 0.9 to 103 Oe for the s-Py17 and from 1.1 to 24 Oe for the s-Py86. Figure 3.9(c) and (d) show the magnetization curves of the s-Py17 and the s-Py86 after pressing at 0.50 MPa. Figure 3.9(e) and (f) show the magnetization curves of the s-Py17 and the s-Py86 after pressing at 0.25 MPa. As can be seen from the s-Py17 in Figure 3.9(a), (c) and (e), the magnetic properties of the s-Py17 are obviously influenced by the pressure. The similar behavior was also observed for the s-Py86 (see Figure 3.9(b), (d) and (f)). Figure 3.10 shows the magnetization curves for the s-Py17 and the s-Py86 prepared by the thermal pressing at 1.0 MPa. The changes in the magnetization curve of Py films after thermal pressing process were also observed using a MPMS measurement.

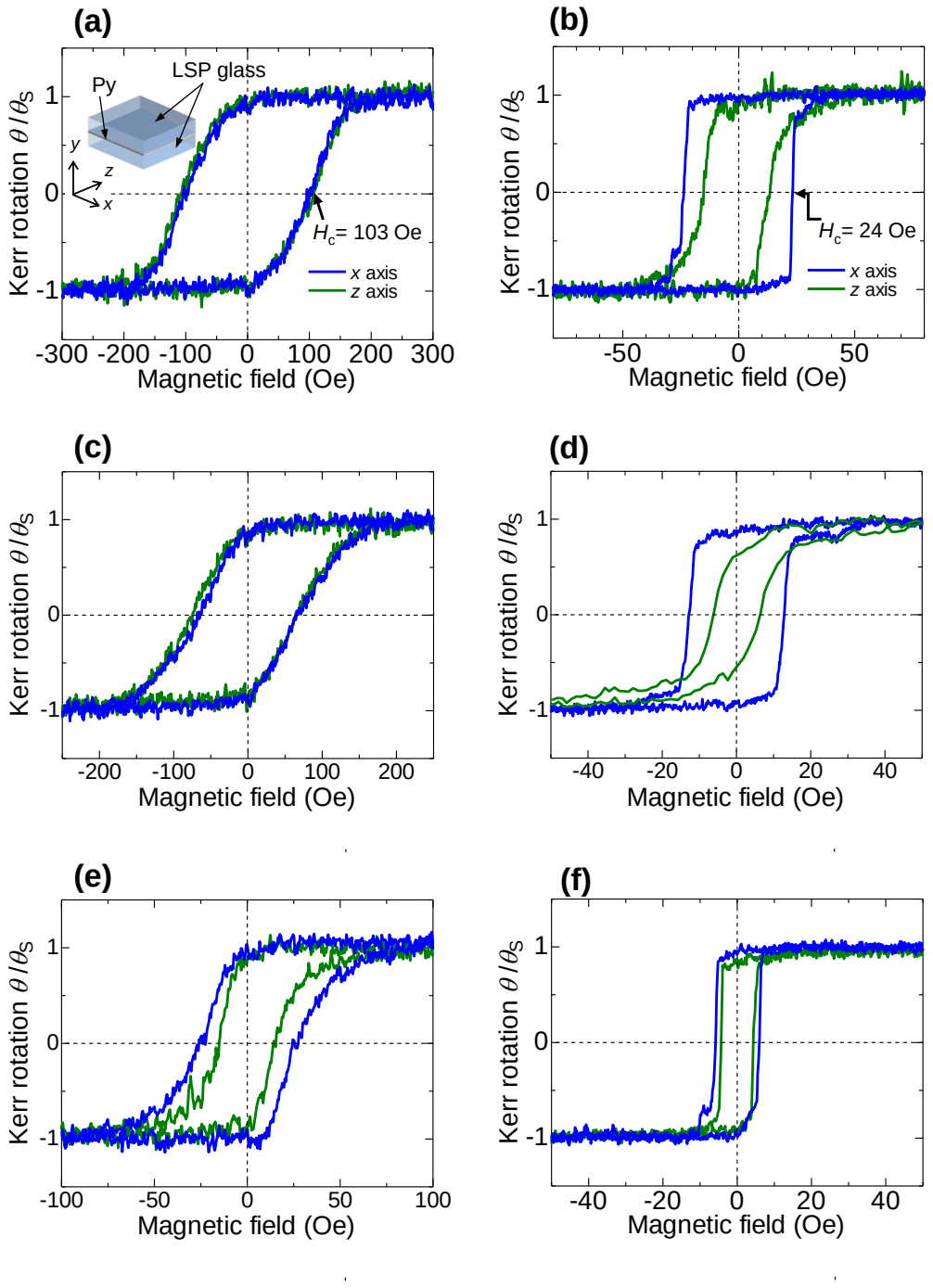

Figure 3.9 Magnetization curves of LSP-glass/Py/LSP-glass; (a) s-Py17 and (b) s-Py86 after 1.0 MPa, (c) s-Py17 and (d) s-Py86 after 0.5 MPa, (e) s-Py17 and (f) s-Py86 after 0.25 MPa.

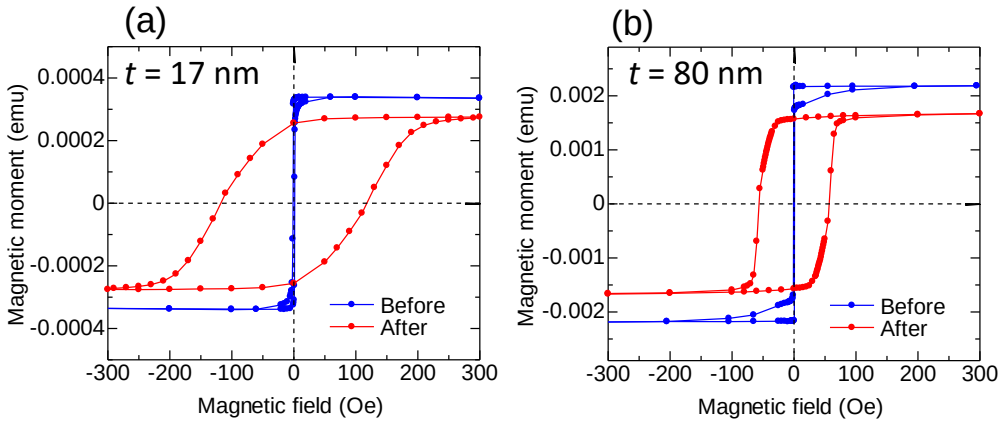

Figure 3.10 Magnetization curves of (a) s-Py17 and (b) s-Py80 before and after pressing at 1.0 MPa observed using MPMS measurement.

Figure 3.11 shows the pressure dependence of the coercivity of three kinds of s-Py samples. The Py thin films thicknesses before thermal pressing were 17, 42, and 86 nm. The coercivity increased proportionally with the applied pressure for each sample. The remarkable increase in coercivity was observed in the thinner Py films. The coercivity for the Py films was also influenced by temperature. Figure 3.12 shows the temperature dependence of the coercivity for Py thin films on LSP glasses. The samples were heated up to the predetermined temperature at 2.5°C/s in N_2 atmosphere, and kept for 5 min for 30 s. After that, the samples were cooled down to room temperature at 1°C/s. There is no difference in coercivity for each Py film below 313°C. In contrast, the coercivity increases proportionally with the temperatures higher than 313°C. A remarkable enhancement in coercivity was also observed in the thinner samples, which tendency is consistent with the results of the pressure dependence of the coercivity shown in Figure 3.11.

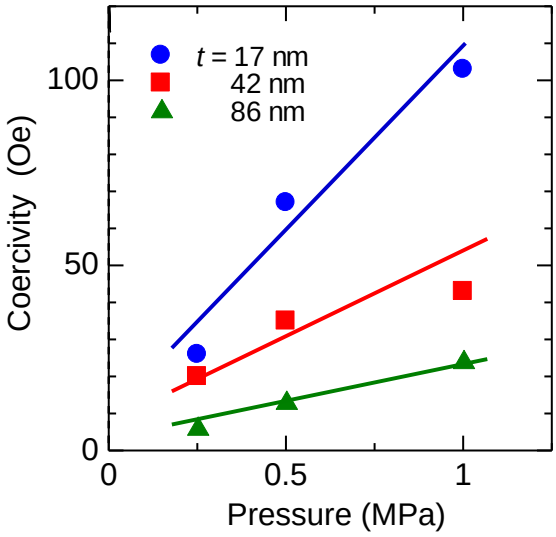

Figure 3.11 Pressure dependence of coercivity of Py thin films with thicknesses of 17, 42, and 86 nm sandwiched between LSP glasses after thermal pressing process.

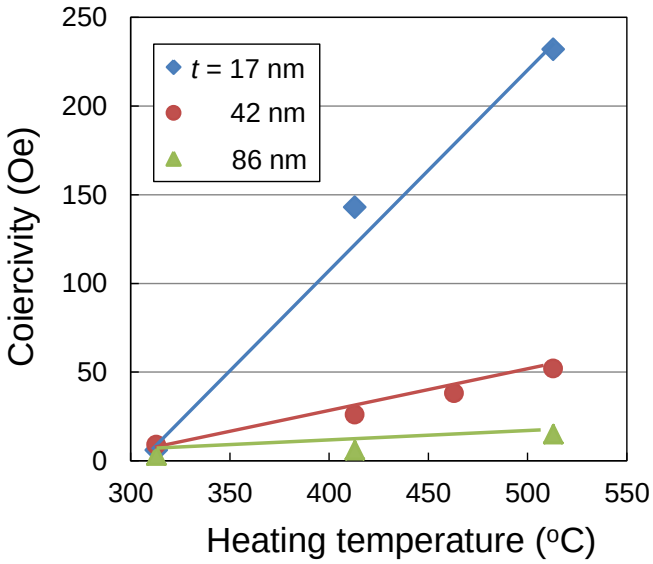

Figure 3.12 Temperature dependence of coercivity of Py thin films on LSP glasses.

3.3.2.3 Mechanism of coercivity enhancement after thermal pressing process

As described in the previous section, it was found that the magnetic properties of s-Py samples were strongly dependent on the thermal pressing condition. In order to clarify the origin of the coercivity enhancement, I investigated the structural properties of the Py thin films before and after the thermal pressing. Figure 3.13(a) and (b) show the TED patterns for the Py17 and the Py86. The TED patterns of both samples exhibit the ring shapes. These ring patterns indicate the polycrystalline structures with fine grains. The result is consistent with the TEM images shown in Figure 3.3(c) and (d). Figure 3.13(c) and (d) show the TED patterns for the s-Py17 and the s-Py86, respectively. The TED patterns of both samples show clear spots, indicating the decrease of grains number (i.e., the increase of crystal grain size). Since the ring patterns were not observed in the probing area (~100 nm) for s-Py17, I concluded that the crystal grain size increased to ~100 nm in this sample after a thermal pressing. This is consistent with the highly oriented crystalline structures observed in Figure 3.8(c).

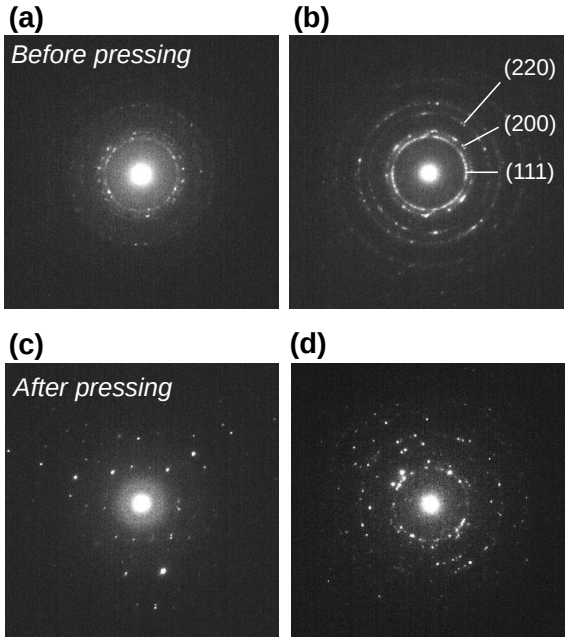

Figure 3.13 Diffraction patterns of (a) Py17, (b) Py86, (c) s-Py17, and (d) s-Py86.

To obtain a quantitative understanding of the grain size, I carried out an XRD measurements of Py thin films. Because the diffraction intensity of the Py17 was so weak, the measurement was carried out for Py86. Figure 3.14 shows the XRD spectra of Py86 before and after thermal pressing at 1.0 MPa. The average crystal grain size in Py thin films can be estimated using Scherrer's equation from the full width at half maximum of the peak in the XRD spectrum. Table 3.1 shows the average crystal grain sizes in the (111), (200), and (220) planes estimated by Scherrer's equation. The average crystal grain size increased by 2.1–3.4 times in each plane after thermal pressing. This finding is consistent with the TEM images in Figure 3.3(d) and Figure 3.8(d) and the TED patterns in Figure 3.13(b) and (d).

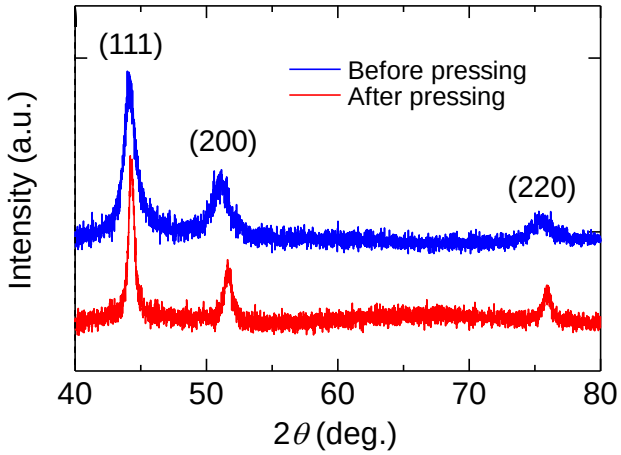

Figure 3.14 XRD spectra of Py86 before and after thermal pressing at 1.0 MPa.

Table 3.1 Average crystal grain sizes of Py86 before and after thermal pressing (denoted by $l_{g,before}$ and $l_{g,after}$).

Crystal plane	(111)	(200)	(220)
$l_{g,before}$	8.5 nm	5.9 nm	5.1 nm
$l_{g,after}$	17.8 nm	14.0 nm	17.1 nm

Now, I discuss the relationship between the grain size and the coercivity in Py thin films. The grain size dependence of coercivity in magnetic *bulk* materials with nanocrystalline structures can be explained by the theoretical calculation based on the three-dimensional (3D) random anisotropy model shown in Figure 3.15 [10, 11]. This model can be extended to the case of magnetic thin films with nanocrystalline structures. In the model, the nanosized grains with magnetocrystalline anisotropies K_1, which are randomly oriented, are ferromagnetically coupled in the two-dimensional (2D) magnetic system. The ferromagnetic exchange length L_{ex} of this system is given by

$$L_{\mathrm{ex}} = \left(\frac{A}{\langle K \rangle}\right)^{\frac{1}{2}}, \tag{3.1}$$

where A is the exchange stiffness constant, and $\langle K \rangle$ is the anisotropy energy density. Since $\langle K \rangle$ indicates the mean fluctuation amplitude of the anisotropy energy of $N\ (= (L_{ex}/l_g)^2)$ grains, where l_g is the crystal grain size, $\langle K \rangle$ can be expressed by

$$\langle K \rangle = \frac{K_1}{\sqrt{N}} = \frac{K_1 l_g}{L_{\mathrm{ex}}}. \tag{3.2}$$

Substituting the equation (3.1) in the equation (3.2) yields $\langle K \rangle = K_1^2 {l_g}^2 / A$. Therefore, the coercivity is represented by

$$H_{\mathrm{c}} = \frac{2K_1^2 {l_g}^2}{M_{\mathrm{S}} A}, \tag{3.3}$$

where M_{s} is the saturated magnetization. The equation (3.3) indicates that the coercivity increases proportionally with ${l_g}^2$. As shown in Figure 3.7(a) and 3.9(a), the coercivity of Py17 was enhanced

from 0.9 to 103 Oe after a thermal pressing. Based on the above-mentioned XRD and TED result, the grain size in this sample was considered to have increased from 8.5 to ~100 nm after a thermal pressing. This change corresponds to a coercivity enhancement of two orders of magnitude for a grain size enhancement of one order of magnitude, which is consistent with the equation (3.3) (i.e., $H_c \propto {l_g}^2$). Same interpretation can be applied to the case of Py86. As shown in Figure 3.7(b) and 3.9(b), the coercivity of Py86 was enhanced from 1 to 24 Oe after a thermal pressing. Simultaneously the grain size increased from 8.5 to 17.8 nm (Table 3.1). Therefore, the relationship between the coercivity and the grain size was represented by $H_c \propto {l_g}^{4.3}$. According to the 3D random anisotropy model, the coercivity in magnetic *bulk* materials is given by $H_c \propto {l_g}^6$. Because the 86-nm-thick films are regarded as materials between 2D and 3D systems, it is reasonable that the exponential value γ in $H_c \propto {l_g}^{\gamma}$ is 4.3 because $2 < \gamma < 6$. In summary, these results suggest that the enhancement in coercivity after thermal pressing can be attributed to the increase in crystal grain size with random magnetic anisotropy.

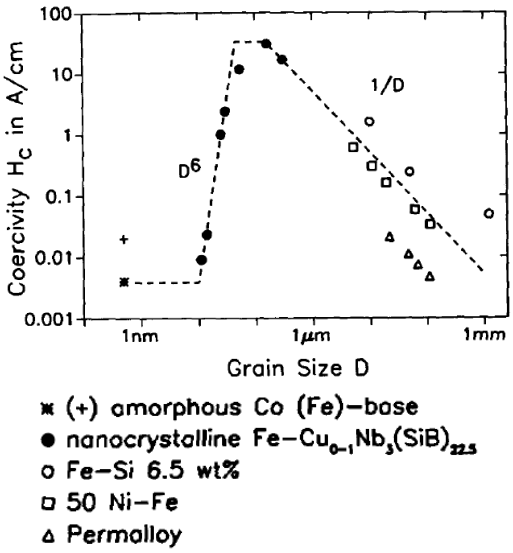

Figure 3.15 Relation between grain size and coercivity for various soft magnetic metallic alloys (Ref. 11).

Figure 3.16(a) and (b) show the AFM images of polished cross-sectional surfaces of s-Py17 and s-Py86. Py thin-film edges can be confirmed at the centers of the scanning areas. The roughnesses in the 500×500 nm^2 area of the polished surfaces were as small as 0.42 and 1.2 nm for s-Py17 and s-Py86, respectively. The R_q of the polished surface of s-Py17, which was estimated as 0.42 nm, is almost the same as that of s-Co14 (0.44 nm) [9]. Although the Py thin-film edges are convex upward for a few nm, this edge structure enables a good contact between the Py edges and the sandwiched materials in the junction of SQC devices. Figure 3.16(c) and (d) show the MFM images of the same specimens shown in (a) and (b), respectively. The stray magnetic field was generated along the out-of-plane direction from the Py thin-film edges. The stray field makes it possible to generate a local field between the two film edges in SQC devices. These results indicate that Py thin films sandwiched between LSP glasses can be used for electrodes of SQC devices from the viewpoint of structural and magnetic properties.

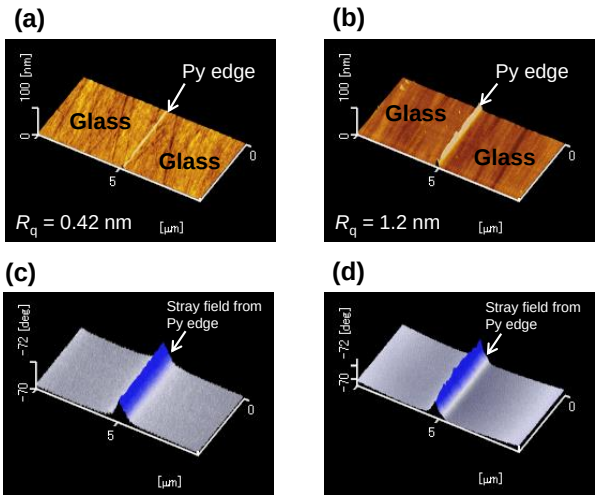

Figure 3.16 AFM images of polished cross-sectional surfaces of (a) s-Py17 and (b) s-Py86 and their MFM images of (c) s-Py17 and (d) s-Py86. The pressure during thermal pressing is 1.0 MPa.

Here, I discuss the influence of CMP method on the structural and magnetic properties for a prospective use of SQC devices. There is a possibility for the polishing in air (atmospheric pressure) to oxidize the Py edge surfaces. Such oxidation can provide a significant influence on the structural and magnetic properties in SQC devices. The oxidation of Ni to NiO is expected to proceed on the edge surface. The oxidations of Fe to α-Fe_2O_3, γ-Fe_2O_3 and Fe_3O_4 are also possible. Since NiO and α-Fe_2O_3 are antiferromagnetic and γ-Fe_2O_3 and Fe_3O_4 are ferrimagnetic at room temperature, these formations cause the reduction of magnetization of Py edges. Weaker stray field generated from the edges degrades the spin filter effect in SQC devices. From a perspective of such structural and magnetic properties, the investigation of Py edge surface is of great importance to obtain a large spin filter effect. If a perfect Py edge surface was not obtained in the wet process, a dry process, such as ion etching in vacuum, could be useful for the removal of oxide layer as a final process of edge treatment, which leads to the achievement of a large spin filter effect.

3.3.2.4 Calculation of stray magnetic field between crossed edges of two Py thin films

Finally, I show the calculation results of the stray field generated between two edges of Py electrodes in SQC devices and discuss the applicability of Py thin films in spin-filter devices. Figure 3.17(a) shows the structure of an SQC device for calculating the stray field generated between crossed edges of two Py electrodes. The magnetization of Py was set to 859 emu/cc. The Py thickness $t_{y(z)}$ was 5–20 nm, and the distance between the two Py electrode edges d was 5–20 nm. The origin of (x, y, z) coordinates was chosen in the center of junction. Figure 3.17(b)–(d) shows the calculation results of stray field at z = 0 nm. For $t_{y(z)}$ = 5 and 20 nm at d = 20 nm, showing in Figure 3.17(b) and (c), the stray field was low (2–4 kOe), and a uniform distribution was not obtained. In contrast, as shown in Figure 3.17(d), the stray field measured as high as 5 kOe. A uniform

distribution was successfully obtained for $t_{y(z)}$ = 20 nm and d = 5 nm. Figure 3.17(e) shows the stray field in the center of the junction as a function of Py thickness. This figure indicates that a high stray field of around 5 kOe was generated when the distance between two Py electrode edges was less than 5 nm. The Py thickness was greater than 20 nm. This high magnetic field produces a large Zeeman effect in the sandwiched materials between two edges of the magnetic thin-film electrodes. The Zeeman splitting energy ΔE_H can be expressed by $2g\mu_B SH$, where g is the g-factor of electrons, μ_B is the Bohr magneton (58 μeV/T), S is the spin quantum number, and H is the magnetic field. Here, g is almost equal to 2.0 and H is 5 kOe, as obtained by the above calculation. Because a large spin S of the order of a few hundred to a thousand has been reported in QDs such as MnAs nanoparticles in a GaAs matrix [12], ΔE_H was estimated to be a few 10–100 meV. This large Zeeman splitting produces a large spin-filter effect. Although the stray field in Py-based SQC devices (5 kOe) is almost similar to or slightly smaller than that in Co-based SQC devices (6 kOe) [12], the above estimation reveals that a stray field of 5 kOe is enoughly high to obtain a large spin filter effect. These experimental and calculated results suggest that Py thin film around 20 nm thickness sandwiched between LSP glasses can be used as an electrode in SQC device, providing a spin-filter effect. The proposed techniques utilizing magnetic thin-film edges will also open up new opportunities for the creation of high performance spin devices, such as large magnetoresistance devices and nanoscale spin injectors.

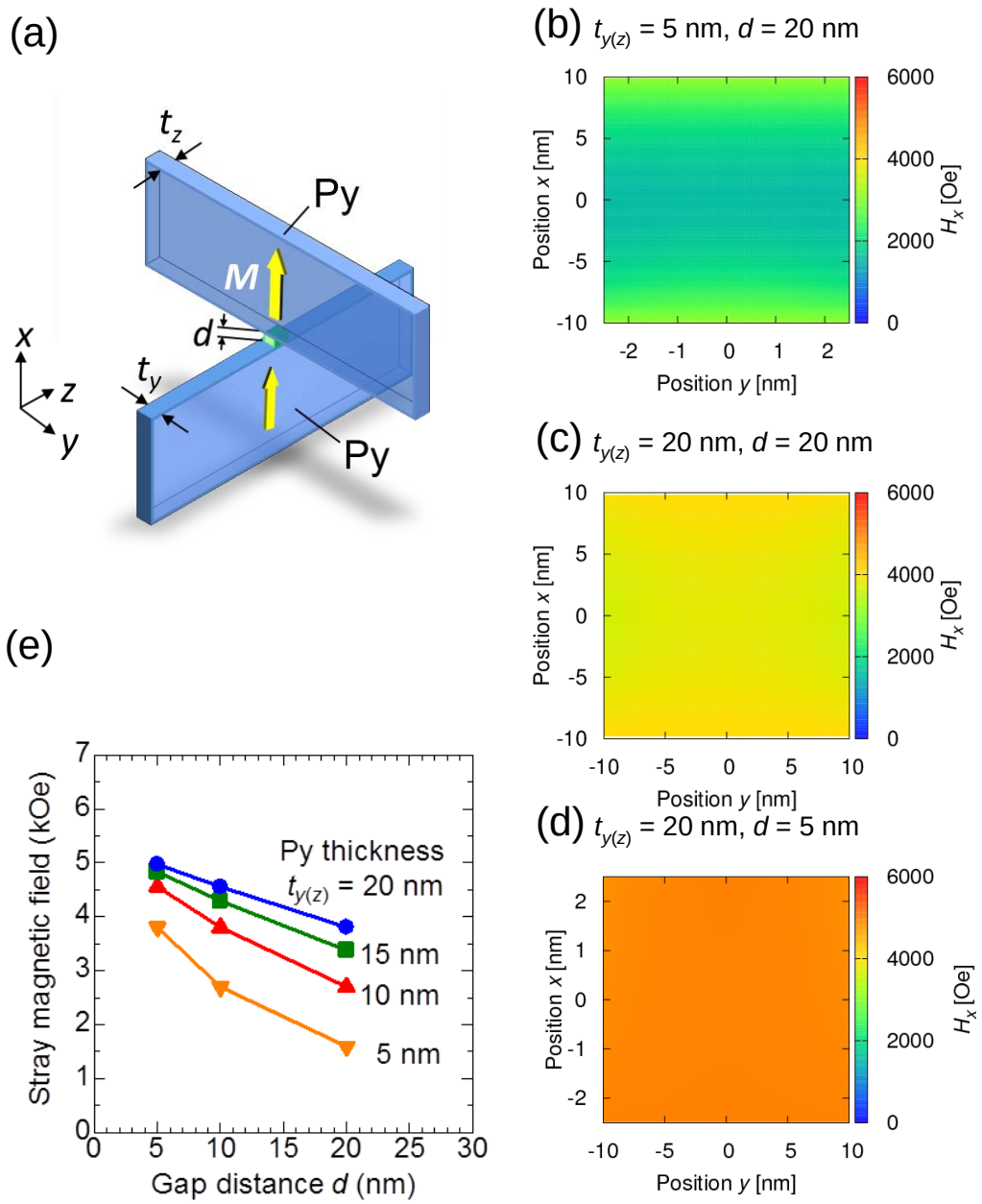

Figure 3.17 (a) SQC device structure for stray field calculation between two edges of Py thin-film electrodes. Results of stray field calculation for the junction of SQC devices with (b) $t_{y(z)}$ = 5 nm and d = 20 nm, (c) $t_{y(z)}$ = 20 nm and d = 20 nm, and (d) $t_{y(z)}$ = 20 nm and d = 5 nm. (e) Stray field in center of junction as a function of Py thickness.

3.4 Conclusion

In this chapter, I investigated the structural and magnetic properties of Py thin films sandwiched between LSP glasses, which can be used in SQC devices. I was successfully fabricated LSP-glass/Py/LSP-glass structures with smooth and clear interfaces. The coercivity of Py thin films was drastically enhanced from 0.9 to 103 Oe after thermal pressing. According to a TEM and TED observations, XRD measurements, and theoretical calculations based on the random anisotropy model, this coercivity enhancement can be explained by the increase in crystal grain size with random magnetic anisotropy. A uniform stray magnetic field was also observed from the Py thin-film edge in the direction perpendicular to the cross section of the LSP-glass/Py/LSP-glass structures. The micromagnetic simulation results indicated that a high stray field of around 5 kOe was generated when the distance between the two Py thin-film electrode edges was less than 5 nm, and the Py thickness was larger than 20 nm. These experimental and calculated results promise that Py thin films sandwiched between LSP glasses are useful as the electrodes of SQC devices, which serve as spin-filter devices.

3.5 References

1. G. Chin, *IEEE Trans. Magn.* **7** (1971) 102.
2. A. Slachter, F. L. Bakker, J. P. Adam, and B. J. van Wees, *Nat. Phys.* **6** (2010) 879.
3. Y. Fukuma, L. Wang, H. Idzuchi, S. Takahashi, S. Maekawa, and Y, Otani, *Nat. Mater.* **10** (2011) 527.
4. P. Tyagi, E. Friebe, C. Baker, *NANO* **10** (2015) 1530002.
5. P. Saravanan, J. H. Hsu, C. L. Tsai, A. K. Singh, and P. Alagarsamy, *IEEE Trans. Magn.* **51** (2015) 2006604.
6. P. Thangadurai, Y. Lumelsky, M. S. Silverstein, and W. D. Kaplan, *Mater. Charact.* **59** (2008) 1623.
7. A. Thran, T. Strunskus, V. Zaporojtchenko, and F. Faupel, *Appl. Phys. Lett.* **81** (2002) 244.
8. H. Kaiju, N. Basheer, K. Kondo, and A. Ishibashi, *IEEE Trans. Magn.* **46** (2010) 1356.
9. H. Kaiju, H. Kasa, T. Komine, S. Mori, T. Misawa, T. Abe, and J. Nishii, *J. Appl. Phys.* **117** (2015) 17C738.
10. A. Alben, J. J. Becker, and M. C. Chi, *J. Appl. Phys.* **49** (1978) 1653.
11. G. Herzer, *IEEE Trans. Magn.* **26** (1990) 1397.
12. P. N. Hai, S. Ohya, M. Tanaka, S. E. Barnes, and S. Maekawa, *Nature* **458** (2009) 489.

Chapter 4

Fabrication and characterization of nanoscale junctions utilizing thin-film edges

4.1 Introduction

In the previous chapters, I successfully established the fabrication method of ultra-flat LSP-glass/Py/LSP-glass cross-sectional structure. Based on this finding, the molecular nanoscale junction devices, which consist of molecules sandwiched at the orthogonal cross-point between two metal thin films, are fabricated in this chapter. The schematic illustration of a metal/molecule/metal nanoscale junction has been already shown in Figure 1.7.

In previous studies, established measurement techniques, such as mechanically controllable break junction (MCBJ) [1−4] or scanning tunnelling microscopy break junction (STM–BJ) techniques [5], have been mainly used for nanoscale junctions consisting of metal/molecule/metal structures. However, such techniques were difficult to use for the investigation of device properties depending on their junction area ranging from nanometer to micrometer scale.

In this chapter, I fabricate nanoscale junctions consisting of Alq_3 molecules sandwiched at the orthogonal cross-point between two Py thin film edges. The structural and electrical properties of Py/Alq_3/Py nanoscale junctions were investigated. Especially, I focused on their carrier transport properties of Alq_3 at the cross-point, depending on a junction area ranging from nanometer to micrometer scale, leading to the observation of bridging area between quantum states and classical configurations.

4.2 Experimental

4.2.1 Fabrication of nanoscale junction

The fabrication procedure of nanoscale junctions is described in Figure 4.1. First, the LSP glass substrates with dimensions of $10\times10\times2\ mm^3$ were prepared and chamfered on both sides (Figure 4.1(a)). Py thin films with thicknesses of 5–250 nm were deposited on the LSP glasses by an ion-beam sputtering method (Figure 4.1(b)) under the same conditions as described in chapter 3. Afterwards, Au thin films with thickness of 14 nm were deposited only on the chamfered glass edges (Figure 4.1(c)). Py thin films sandwiched between the LSP glasses were fabricated using a thermal pressing machine (Toshiba Machine Co. Ltd., GMP–00504V) under the pressure of 0.25 MPa(Figure 4.1(d)). Other thermal pressing conditions were same as described in chapter 2. The bonded LSP-glass/Py/LSP-glass were cut in half, and their cross-sectional surfaces of were polished (Figure 4.1(e)−(f)). The conditions of cutting and polishing process were described in chapter 3. An Alq_3 film with a thickness of 20 nm was spin-coated on the polished LSP-glass/Py/LSP-glass substrate at a rotation speed of 8000 rpm and processing time of 60 s (Figure 4.1(g)). The Alq_3 solution for spin-coating was prepared by dissolving the Alq_3 powder(Sigma Aldrich; 99.995% pure) in chloroform to form a $1\ mg/mL$ solution. Finally, the polished LSP-glass/Py/LSP-glass surface was stacked on the Alq_3 film at a pressure of 0.14 MPa. The fabricated nanoscale junction is depicted in Figure 4.1(h).

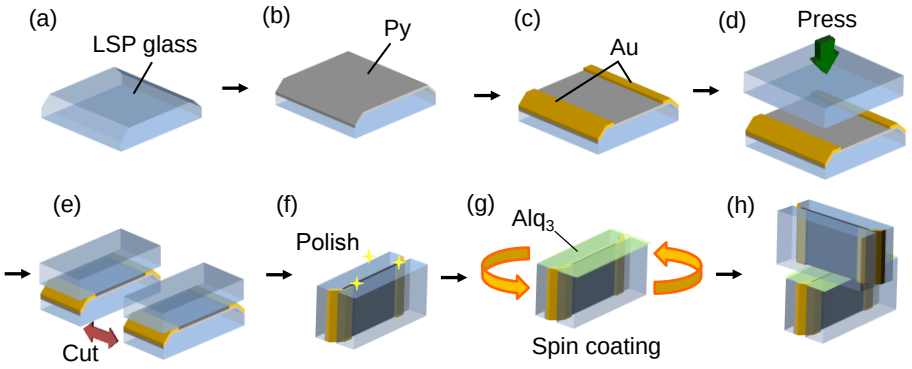

Figure 4.1 Fabrication of Py/Alq_3/Py nanoscale junction; (a) formation of chamfered edges, (b) ion-beam sputtering of Py thin films, (c) sputtering of Au films on chamfered edges (d) thermal pressing of two glasses, (e) cutting, (f) polishing of cross-sectional surface, (g) spin coating of Alq_3 films on polished glass/Py/glass surface, (h) stacking of another glass/Py/glass cross-sectional surface on Alq_3 coated surface.

4.2.2 Characterization of specimen

The microstructures and interfacial features of the prepared LSP-glass/Py/LSP-glass substrates were examined using TEM, TED, and EDS techniques in the same manner as described in chapter 3. Also, the Py thin film thicknesses were estimated from the TEM views ,a stylus surface profiles and the transmittance estimated using a Lambert-Beer method. The detail estimation methods are described in chapter 3.

Surface morphologies and roughnesses of the polished LSP-glass/Py/LSP-glass structures were analysed using an AFM (SII Nano Technology Inc., Nanocute). The electrical properties of Py thin film edges with and without Alq_3 were evaluated using a conductive-AFM (cAFM) instrument equipped with an Rh-coated cantilever (Si–DF3–R). The structure of Alq_3 was determined using a Fourier-transform infrared spectroscopy (FT–IR) (JASCO Corporation, FT/IR–6300V) and a photoluminescence spectroscopy (PL) (Hamamatsu Photonics K.K., Quantaurus–QY). Molecular orbital energies of Alq_3 molecule were calculated using a density functional theory (DFT) calculations based on the B3LYP/6-31+G(d) method, the Gaussian 09 software. The resistance of Py

electrodes in the fabricated Py/Alq_3/Py nanoscale junctions was measured using a two-probe method at room temperature. The current–voltage (*I–V*) characteristics of the junctions were evaluated using a four-probe method at room temperature.

4.3 Results and Discussion

4.3.1 Characterization of Py thin-film edge used in nanoscale junction

Figure 4.2(a) shows the cross-sectional bright-field TEM images and TED pattern obtained for an 11-nm thick Py film sandwiched between the LSP glasses. The film with smooth and clear interfaces can be successfully formed over areas exceeding 1 μm. The TED patterns of Py film in a probing area of around 100 nm in diameter show clear spots, indicating a highly oriented crystalline structure. The formation of 11-nm thick Py film is of great importance because the film thickness directly determines the junction area. Namely, the orthogonal cross-point of 11-nm thick film edges can produce nanoscale junctions of 11×11 nm^2. Figure 4.2(b) shows the TEM–EDS mapping images of an 86-nm thick Py film sandwiched between the glasses. This particular film thickness was selected because the EDS intensity obtained for 11-nm thick Py films is typically low. The cross section exhibited smooth and clear interfaces without any diffusion of Ni and Fe atoms into the bulk glass. It should be noted that in some cases, metal atoms diffuse into LSP materials after deposition [6−10]. For example, Au deposited on a pentacene thin film diffused inside and accumulate on the interface surface; a low Au deposition rate of around 0.1 Å/s led to the formation of a broad interface between Au and pentacene layers, which was indicated by the cross-sectional SEM studies [6,7]. In another work, high-resolution TEM observations revealed that the interfacial region was observed between deposited Al thin film and P3HT:PCBM blend regardless of the thermal treatment [8, 9]. In contrast to the results presented above, such metal diffusion into the bulk of LSP materials did not occur at the interface between Py and LSP glass in this study.

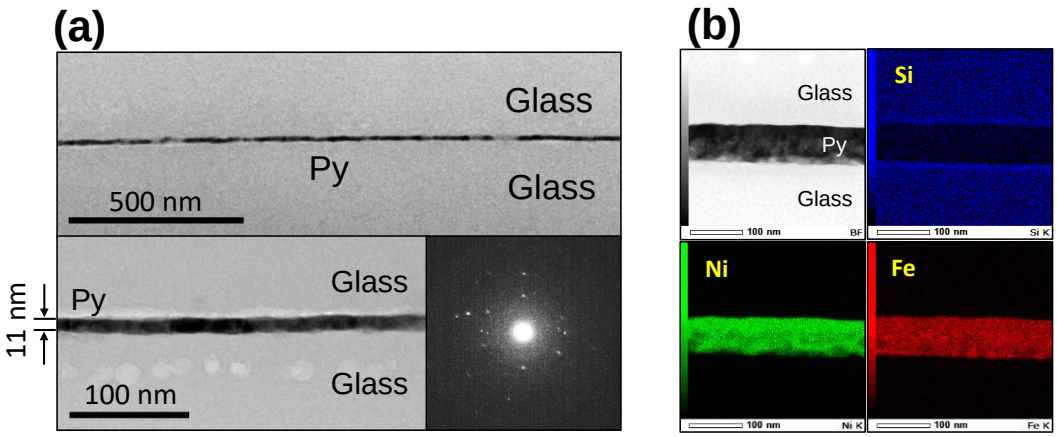

Figure 4.2 TEM, TED, and EDS studies LSP-glass/Py/LSP-glass structure. (a) Cross-sectional TEM images and TED pattern obtained for 11 nm thick Py film sandwiched between LSP-glasses. (b) TEM and EDS mapping images of 86 nm thick Py film sandwiched between LSP-glasses.

The same behavior was also observed for a 220 nm thick Py film described in Figure 4.3. Figure 4.3(a) shows the cross-sectional bright-field TEM images of the 220 nm thick Py film sandwiched between two LSP glasses. Smooth and clear Py/LSP-glass interfaces can be successfully formed without any diffusion of Ni and Fe atoms into the LSP glass. Figure 4.3(b) shows the TED pattern obtained for a probing area of around 100 nm for the same specimen. The TED pattern shows clear spots, suggesting that the sample possesses a highly oriented crystalline structure. The obtained TEM and TED results revealed the formation of grains with relatively large sizes of around 50 nm in diameter, which were consistent with the results depicted in Figure 4.2(a). In addition, it is also emphasized that the orthogonal cross-point of 220-nm thick Py film edges forms the junction area of 220×220 nm^2. These results indicate that the Py thin films sandwiched between LSP glasses can be used as electrodes not only the nanoscale junctions, but also of the sub-micron ones led to the observation.

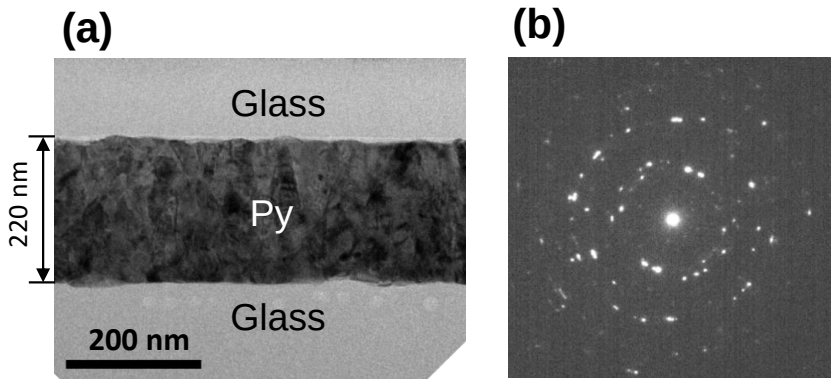

Figure 4.3 TEM and TED images of LSP-glass/Py/LSP-glass structure. (a) Cross-sectional TEM image of 220 nm thick Py thin film sandwiched between LSP glasses. (b) TED pattern obtained in the center portion of Py film.

Figure 4.4(a) shows the AFM images of the polished cross-sectional surfaces of the glass/Py (15 nm)/glass. The upper image depicts the A–B line profile of corresponding 2D image, which confirmed at the center of Py thin-film edge. The polished surface roughness measured over the scanning area of 500×500 nm^2 was less than 0.42 nm. The observed Py thin-film edge exhibited a convex shape with a height of around 5.3 nm. The convex shape ensures a good contact between orthogonally crossed Py edges and the sandwiched material, that is Alq_3 in this study, in nanoscale junctions. The projected edge height can be controlled during the second step of the CMP process using SiO_2 slurries. Figure 4.4(b) shows the 2D- and 3D-cAFM images of the same specimen, indicating the uniform electrical conduction along the Py edges. Figure 4.4(c) shows the *I–V* characteristics obtained at an arbitrary position of the Py edges before and after the optimization of polishing conditions. Before the optimization, the tunnelling behavior was observed, indicating the presence of an oxide layer on the Py edge surface. According to Simmons' equation [11], the current density *J* in metal/insulator/metal tunnel junctions can be expressed by

$$J = \frac{e}{2\pi ht^2}\left[(\phi - \frac{eV}{2})\exp\left(-\frac{4\pi t}{h}\sqrt{2m(\phi - \frac{eV}{2})}\right) - (\phi + \frac{eV}{2})\exp\left(-\frac{4\pi t}{h}\sqrt{2m(\phi + \frac{eV}{2})}\right)\right], \quad (4.1)$$

where t is the barrier thickness, ϕ is the barrier height, e is the charge of an electron, h is Planck's constant, V is the applied voltage, and m is the electron mass. When an oxide layer is present on the Py edge surface, the I–V characteristics obey the equation (4.1). After the fitting procedure, it was found that t = 1.3 nm and ϕ = 0.96 eV, indicating that an oxide layer with a thickness of 1.3 nm could be formed on the Py edge before the optimization of polishing conditions. In contrast, ohmic characteristics were observed after the optimization, suggesting that the oxidized layer was not remained.

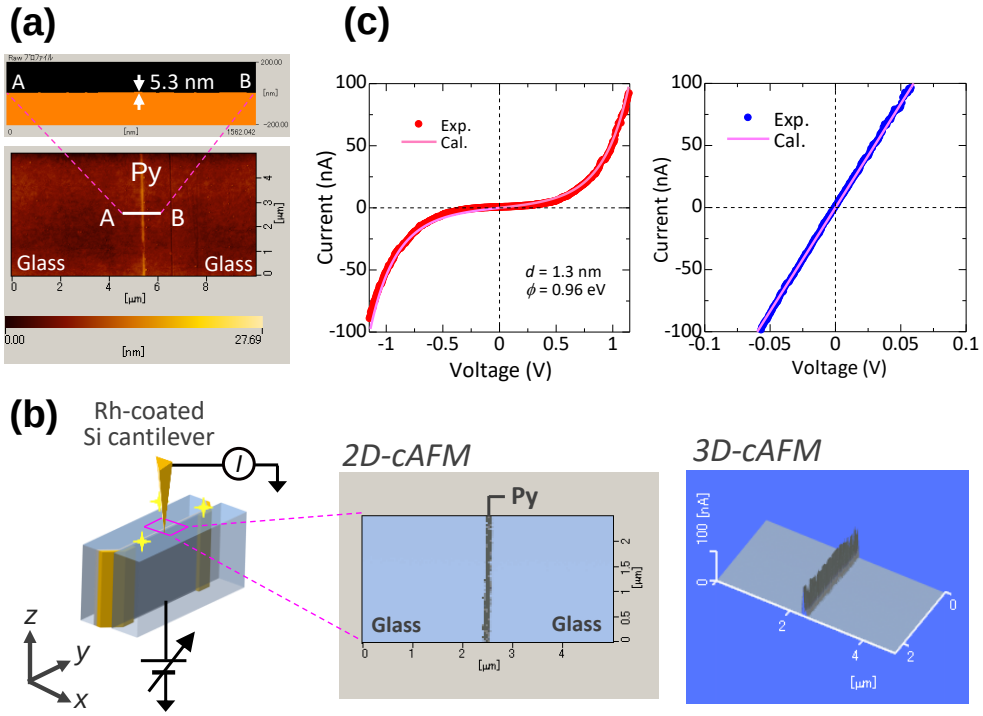

Figure 4.4 AFM and cAFM images of polished LSP-glass/Py/LSP-glass cross-sectional surface. (a) AFM images of polished surfaces (b) 2D- and 3D-cAFM images obtained for LSP-glass/ Py(15 nm)/LSP-glass substrate. (c) I–V characteristics of Py edge obtained before (left) and after (right) optimization of polishing conditions.

In my previous study described in the chapter 2, the contrast enhancement of Co edge, which was attributed to its high conductivity, was observed for SEM images of LSP-glass/Co (14 nm)/LSP-glass [12]. However, uniform electrical conduction as well as ohmic behavior was not observed during cAFM studies of Co samples, suggesting the formation of a thin oxide layer on the Co edge surface. The obtained results indicate that Py exhibits better long-term stability and oxidation resistance properties than those of Co.

4.3.2 Characterization of Alq_3 film

Figure 4.5(a) shows the FT-IR spectra recorded for a 20 nm thick Alq_3 film. The spectrum was obtained using a reflection absorption spectroscopy. In order to obtain an intense IR absorption, the Alq_3 film was spin-coated onto a 200 nm thick Ni film, which had been previously evaporated onto a glass substrate. The measured FT-IR intensities were in good agreement with the reference data for Alq_3 [13], indicating the formation of high-quality Alq_3 thin films. In order to determine the Alq_3 structure (*mer*-Alq_3 or *fac*-Alq_3 [14] one), PL spectra were measured for a 20 nm thick Alq_3 film. The PL peak depicted in Figure 4.5(b) was detected at a wavelength of 525 nm, corresponding to green emission, which suggested that the structure of Alq_3 was identified as the meridional type. The obtained experimental results have also supported confirmed by the DFT calculations conducted using a B3LYP/6-31+G(d) method. Then, the *mer*-Alq_3 thin film was spin-coated on the polished glass/Py (17 nm)/glass surface, after which the cAFM technique was used to investigate its local conductivity. As shown in Figure 4.5(c), a uniform electrical conduction through the Alq_3 film was observed along the Py edges. The Py edge width was 17 nm, which was equal to the Py thickness estimated by the cross-sectional TEM observations.

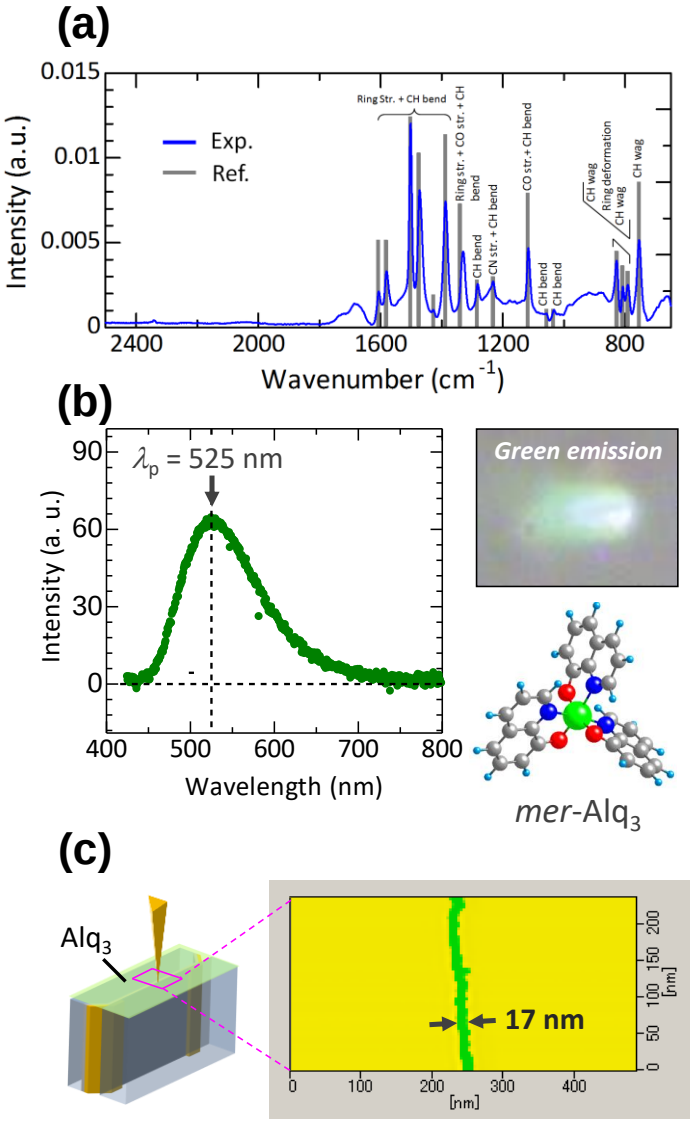

Figure 4.5 Characteristics and cAFM images of Alq_3 film deposited on LSP-glass/Py/LSP-glass cross-sectional surface. (a) FT–IR and (b) PL spectra of 20 nm thick Alq_3 film. (c) 2D-cAFM image of spin-coated Alq_3 film on LSP-glass/Py(17 nm)/LSP-glass cross-sectional surface.

4.3.3 Electrical property of Py/Alq_3/Py nanoscale junction

Using the described techniques, Py/Alq_3/Py nanoscale junctions have been fabricated by sandwiching Alq_3 films between two polished LSP-glass/Py/LSP-glass substrates. The electrical properties of the nanoscale junctions, such as the Py electrode resistance and *I–V* characteristics,

were investigated. Figure 4.6 shows the electrode resistance plotted as a function of linewidth L, which corresponds to the film thickness in the proposed nanoscale junctions. The electrode resistance for conventional cross-bar devices is also shown for comparison purposes. The black solid, dashed, and dotted lines represent the Py electrode resistances estimated for conventional cross-bar devices with electrode aspect ratios of 1:1, 5:1, and 10:1, which were larger than the values of 37, 7.3, and 3.7 MΩ, respectively, obtained at L < 20 nm for $Ni_{80}Fe_{20}$ thin films on glass substrates [15]. In contrast, the electrode resistance values obtained for the proposed nanoscale junctions were relatively small: 0.3−2 kΩ for Ni/PEN samples (see ref. [16]) and 0.04−0.34 kΩ for LSP-glass/Py (or Co)/LSP-glass specimens. Such extremely low resistance values are attributed to their high aspect ratios of over 10^5:1 and low resistivity of Py (or Co) films deposited on LSP glass substrates. The reduction in resistance observed for Py electrodes allows precise detection of the resistance of Alq_3 molecules sandwiched between the two edges of Py thin films.

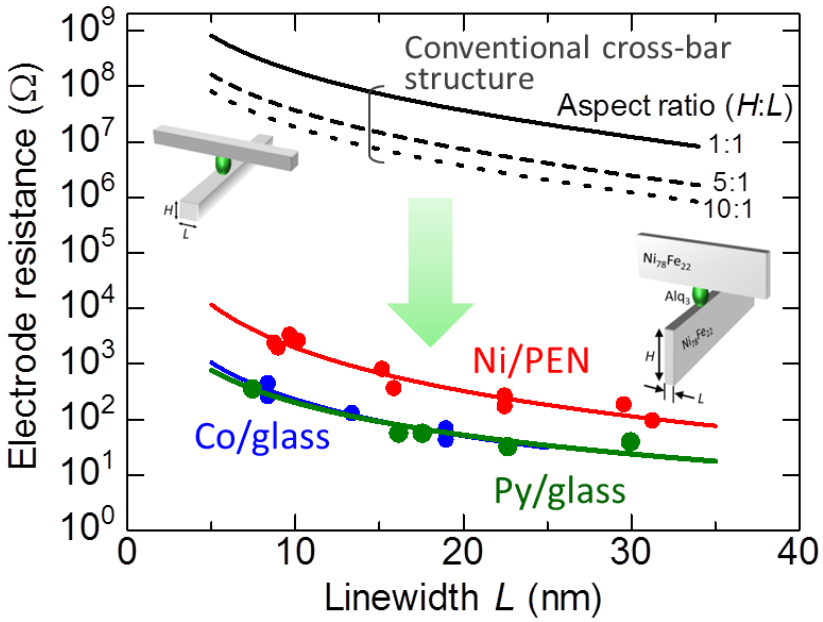

Figure 4.6 Linewidth dependence of electrode resistance in nanoscale junctions.

Figure 4.7 shows the *I*–*V* characteristics of the Py/Alq_3/Py junctions with various junction areas, ranging from nanometer to submicron scales. This figure also contains the *I*–*V* curve for the Co/Alq_3/Co junction with an area of $S = 200\times200$ μm^2, which was fabricated using a thermal evaporation method with mask. The utilized slit width was 200 μm, and the measured thicknesses of top and bottom Co electrodes were 26 and 15 nm, respectively. The thickness of the Alq_3 layer, which was fabricated by spin coating, was 100 nm. Here, it should be noted that the Co/Alq_3/Co junction was selected to investigate the *I*–*V* characteristics because of the diffusion of Ni and Fe atoms into the Alq_3 layers observed after Py deposition.

In Figure 4.7(a), the ohmic characteristic was observed inside the region with a low bias ($|V| \leq 2.2$ V). On the other hand, the dependence $I \propto V^2$ characterized the region with a high bias ($|V| > 2.2$ V). According to Child's law, the transport carriers injected from a metal layer into the trap-free organic layer can exhibit two different regimes: ohmic conductivity at low voltages and the square law dependence at higher voltages, which corresponds to the space-charge-limited current (SCLC) [17,18]. As shown in Figure 4.7(a), this theoretical description is in good agreement with the obtained experimental results. In addition, the current density *J* corresponding to the SCLC magnitude can be generally expressed as $J = 9\epsilon_r\epsilon_0\mu V^2/8d^3$, where ϵ_r is the relative permittivity, ϵ_0 is the permittivity of the vacuum, μ is the carrier mobility, and *d* is the layer thickness. Fitting the obtained curve ($I \propto V^2$) with the SCLC formula using ϵ_r = 3.0 for Alq_3 [19] and *d* = 100 nm yields the carrier mobility $\mu = 1.6\times10^{-5}$ cm^2/Vs, which agrees well with the reported value for bulk Alq_3 (~10^{-5} cm^2/Vs) [20]. The obtained results indicate the successful formation of a high-quality trap-free Alq_3 layer with high conductivity.

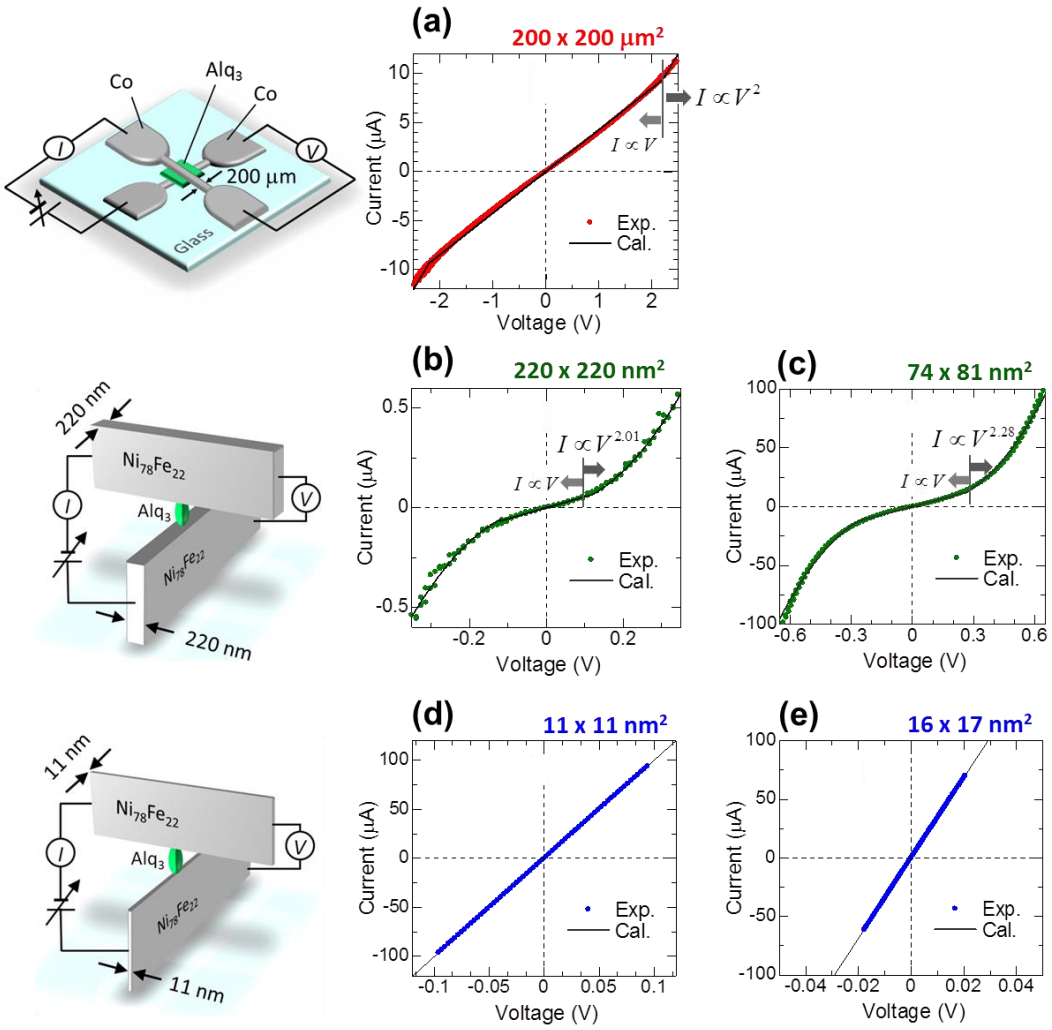

Figure 4.7 *I*–*V* characteristics of metal/Alq_3/metal junctions. (a) Co/Alq_3/Co junction with area of 200×200 μm^2. Py/Alq_3/Py nanoscale junctions with junction area of (b) 220×220 nm^2, (c) 74×81 nm^2, (d) 11×11 nm^2 and (e) 16×17 nm^2.

Figure 4.7(b) shows the *I*–*V* characteristics obtained for the Py/Alq_3/Py junctions, which were fabricated utilizing the Py thin-film edges. The thickness of the Py films were 220 nm; therefore, the junction area was equal to $S = 220\times220$ nm^2. Ohmic characteristic was observed for these junctions at low voltages ($|V| \le 0.1$ V), and the $I \propto V^{2.01}$ dependence at higher voltages ($|V| > 0.1$ V). A similar behavior was also observed for the junctions with $S = 74\times81$ nm^2, which exhibited the ohmic characteristic at low voltages ($|V| \le 0.26$ V) and the $I \propto V^{2.28}$ dependence at

higher voltages ($|V| > 0.26$ V) (Figure 4.7(c)). The voltage exponents in the relations obtained at higher voltages were 2.01 and 2.28, which were close to the value of 2.0, indicating that nearly trap-free carrier transport, described by SCLC, can be achieved for Alq_3 layers.

Figure 4.7(d) shows the *I*–*V* characteristics of the Py/Alq_3/Py junctions with $S = 11 \times 11$ nm^2, which correspond to the ohmic behavior with a junction resistance of 1 kΩ. The measured resistance was much smaller than the estimated value of around 10^{13} Ω, which was obtained from the Ohm's law; the resistivity ρ of bulk Alq_3 estimated from the slope of the *I*–*V* curve at low voltages (see Figure 4.7(a)) was assumed to be 1.0×10^5 Ω·m. The observed significant difference in resistance can be attributed to the quantization of conductance. It is well known that the conductance of metal/molecules/metal nanoscale junctions can be quantized in units of $G_0 (= 2e^2/h)$, which is equal to $(12.9\ \text{k}\Omega)^{-1}$, where *e* is the charge of an electron, and *h* is Planck's constant [1−5].

In previous studies, the quantized conductance has been observed for various kinds of molecular junctions by established conduction measurement methods, such as STM–BJ techniques. For example, quantized conductance was systematically investigated via STM–BJ for thiol-, amine-, and carboxylic acid-terminated molecules sandwiched between Au electrodes; the obtained results showed the conductance increase from 10^{-5} to $10^{-3}\ G_0$ in the order of Au−COOH < Au−NH_2 < Au−S [5]. In another work, a high conductance magnitude (typically $0.7G_0$) was observed via MCBJ for metal-carbon coupled materials, such as C_{60}, benzene, and π-stacked benzene deposited on Pt [1], Ag [2], and Au [3] electrodes. From the conductance channel perspective, multiple conductance channels as well as a high conductance of more than $0.1G_0$ were detected by MCBJ for the terthiophenedithiol or terthiophenediselenol species bridged between Au contacts [25].

The experimental results obtained in this study can be explained by the formation of multiple conductance channels. The dimensions of the *mer*-Alq_3 unit cell shown in Figure 4.5(b) are $a = 0.626$ nm, $b = 1.291$ nm, and $c = 1.473$ nm. Assuming that the *ab* plane of *mer*-Alq_3 is in contact

with the Py edges, the number of conductance channels can be expressed as S/ab, which is equal to approximately 150 channels for $S = 11\times11$ nm^2. According to Landauer's equation, the quantized conductance G can be generally written as $G = G_0 \sum_i^N T_i$, where i is the channel index, T_i is the transmission probability for the i–th channel, and N is the ultimate number of the channels [21, 22]. Assuming that the value of T_i is equal to T (channel-independent), the quantized conductance can be simply expressed as $G = NTG_0$. Therefore, the conductance of one channel, G/N, can be approximated as $0.086G_0$, which corresponds to a relatively high value with a small resistance. A similar behavior was also observed at $S = 16\times17$ nm^2, which exhibited ohmic characteristics with a small resistance of 291 Ω (see Figure 4.7(e)). Since the number of conductance channels N in the junction was 336, the calculated conductance of one channel was equal to $0.13G_0$, which also corresponded to a small resistance. As mentioned above, high conductances of $0.7G_0$ and $0.9G_0$ have been observed for Pt/C_{60}/Pt and Pt/ethylene (or acetylene)/Pt junctions, respectively [1,23], due to the effective hybridization between Pt and molecular orbitals (π and/or di-σ) as well as the large local density of states (DOS) at the Fermi level (E_F) of Pt. Since the local DOS at E_F of NiFe alloy is as large as that of Pt [24], it satisfies one of the conditions for high conductance of Py–Alq_3 systems. The other condition, that is, the effective hybridization between NiFe alloy and Alq_3 molecular orbitals has not been clarified yet. To discuss the origin of the observed high conductance in more detail, further theoretical and experimental studies must be conducted.

Based on the obtained I–V characteristics, a phase diagram has been mapped out for the plot of the resistance versus junction area (R–S plot). Figure 4.8 depicts the R–S plot for metal/Alq_3/metal junctions, in which the solid circles represent the data obtained in this work, and the squares denote the results reported by other groups [25, 26]. All plotted values were converted into resistance at d = 20 nm assuming that linear I–V curves, corresponding to the formula $I = en\eta V/dS$, where n was the carrier density, were observed at low bias voltages. Interestingly, the

obtained *R*–*S* plot contained the following three parts: i) a ballistic regime (blue, $S < 20\times20$ nm^2), ii) a transition region between the ballistic regime and a diffusive scheme (green, 20×20 nm$^2 \leq S < 1\times1$ μm^2), and iii) the diffusive scheme (red, $S \geq 1\times1$ μm^2). In the ballistic regime, the resistance R (= 1/G) is inversely proportional to the junction area S ($\propto$ the channel number N), as indicated by the formula $G = NTG_0$. The figure includes the *R*–*S* lines plotted at different values of T between 0.001 and 1.0. In the diffusive scheme, the *R*–*S* line obeys Ohm's law, which is expressed by the formula $R = \rho d/S$.

Finally, the transition region is described by a characteristic line, which connects the ballistic regime and the diffusive scheme together. This region can be considered a bridging area between the quantum states and the classical configurations, which is observed for the first time for molecular systems. Thus, investigating *R*–*S* phase diagrams can lead to new insights on transport phenomena in the range between the nano- and the micrometre regions. It should also be emphasized that the formation of nanoscale junctions with $S = 11\times11$ nm^2, which is the smallest value ever reported for junctions utilizing thin-film edges, can be successfully demonstrated without using conventional lithographic techniques, such as EB or optical lithography. The proposed method can open new venues in the field of nanotechnology, which would lead to further development of the fundamental laws of physics and chemistry as well as next-generation electronic applications, such as high-density memory devices and high-performance logic circuits.

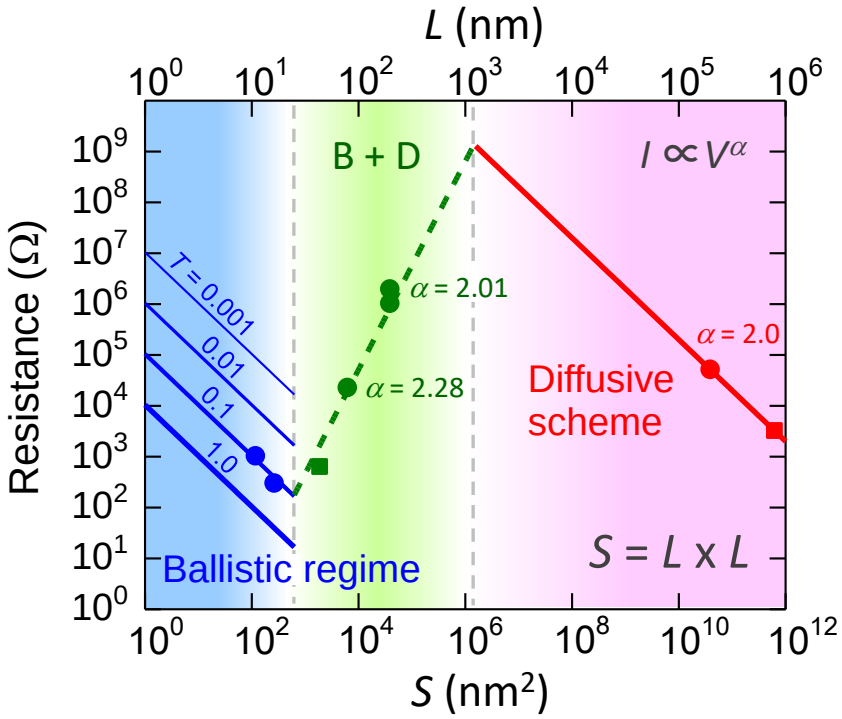

Figure 4.8 Phase diagram containing the plot of resistance versus junction area (R–S plot) for metal/Alq_3(d = 20 nm)/metal junctions.

4.4 Conclusion

I have successfully demonstrated the formation of Py/Alq_3/Py nanoscale junctions with areas of 11×11 nm^2 utilizing thin-film edges without using conventional lithography. The obtained junction area is the smallest value ever reported for such junctions. The I–V curves obtained for these nanoscale junctions exhibited the ohmic behavior, which suggested the formation of multiple quantized conductance channels in the ballistic regime. On the other hand, SCLC was observed in the diffusive scheme for micrometer-size junctions. In addition, the transition region between the ballistic regime and the diffusive scheme was observed for the R–S plot, in which the characteristic line connecting these areas exhibited a linear correlation. This region can be considered a bridging area between the quantum states and the classical configuration. Such behaviour was observed for the first time in molecular systems.

4.5 References

1. M. Kiguchi, *Appl. Phys. Lett.* **95** (2009) 073301.
2. S. T. Schneebeli, M. Kamenetska, Z. Cheng, R. Skouta, R. A. Friesner, L. Venkataraman, and R. Breslow, *J. Am. Chem. Soc.* **133** (2011) 2136.
3. M. Kiguchi, O. Tal, S. Wohlthat, F. Pauly, M. Krieger, D. Djukic, J. C. Cuevas, and J. M. van Ruitenbeek, *Phys. Rev. Lett.* **101** (2008) 046801.
4. K. Yokota, M. Taniguchi, M. Tsutsui, and T. Kawai, *J. Am. Chem. Soc.* **132** (2010) 17364.
5. F. Chen, X. Li, J. Hihath , Z. Huang , and N. Tao, *J. Am. Chem. Soc.* **128** (2006) 15874.
6. J. H. Cho, D. H. Kim, Y. Jang, W. H. Lee, K. Ihm, J. H. Han, S. Chung, and K. Cho, *Appl. Phys. Lett.* **89** (2006) 132101.
7. Y. Xu, C. Liu, H. Sun, F. Balestra, G. Ghibaudo, W. Scheideler, and Y. Y. Noh, *Org. Electron.* **15** (2014) 1738.
8. C. Y. Nam, D. Su, and C. T. Black, *Adv. Funct. Mater.* **19** (2009) 3552.
9. M. Wang, F. Xie, W. Xie, S. Zheng, and N. Ke, *Appl. Phys. Lett.* **98** (2011) 183304.
10. A. Turak, *RSC Adv.* **3** (2013) 6188.
11. J. G. Simmons, *J. Appl. Phys.* **34** (1963) 1793.
12. H. Kaiju, H. Kasa, T. Komine, S. Mori, T. Misawa, T. Abe, and J. Nishii, *J. Appl. Phys.* **117** (2015) 17C738.
13. J. E. Tackett and D. T. Sawyer, *Inorg. Chem.* **3** (1964) 692.
14. M. Goswami, P. K. Nayak, N. Periasamy, and P. K. Madhu, *Chem. Cent. J.* **3** (2009) 1.
15. Y. T. Chen, J. Y. Tseng, S. H. Lin, and T. S. Sheu, *J. Magn. Magn. Mater.* **360** (2014) 87.
16. H. Kaiju, K. Kondo, N. Basheer, N. Kawaguchi, S. White, A. Hirata, M. Ishimaru, Y. Hirotsu, and A. Ishibashi, *Jpn. J. Appl. Phys.* **51** (2012) 065202.
17. A. Rose, *Phys. Rev.* **97** (1955) 1538.

18. M. A. Lampert, *Phys. Rev.* **103** (1956) 1648.

19. J. E. Knox, M. D. Halls, H. P. Hratchian, and H. B. Schlegel, *Phys. Chem. Chem. Phys.* **8** (2006) 1371.

20. V. A. Dediu, L. E. Hueso, I. Bergenti1, and C. Taliani, *Nat. Mater*. **8** (2009) 707.

21. R. Landauer, IBM J. Res. Dev. **1** (1957) 223.

22. B. J. Van Wees, H. van Houten, C. W. J. Beenakker, D. van der Marel, and C. T. Foxon, *Phys. Rev. Lett.* **60** (1988) 848.

23. T. Nakazumi, S. Kaneko, R. Matsushita, and M. Kiguchi, *J. Phys. Chem. C* **116** (2012) 18250.

24. P. H. Dederichs and R. Zeller, *J. Magn. Magn. Mater.* **100** (1991) 241.

25. S. Pramanik, C.G. Stefanita, S. Patibandla, S. Bandyopadhyay, K. Garre, N. Harth, and M. Cahay, *Nat. Nanotech.* **2** (2007) 216.

26. Y. Liu, S. M. Watson, T. Lee, J. M. Gorham, H. E. Katz, J. A. Borchers, H. D. Fairbrother, and D. H. Reich, *Phys. Rev. B* **79** (2009) 075312.

Chapter 5

General Conclusion

In this thesis, I developed the new fabrication technique for metal/molecule/metal nanoscale junctions utilizing metal-thin-film edges. In particular, it was found that $Ni_{78}Fe_{22}$ thin films sandwiched between low-softening-point (LSP) glasses were useful as electrodes for my proposed nanoscale junctions. The main results are summarized as follows.

First, Co thin films sandwiched between LSP glasses were fabricated using a thermal pressing technique and a multi-step polishing method. Their structural and magnetic properties were investigated (Chapter 2). As a result, it was successfully demonstrated that the structures with smooth Co thin films and flat Co edges were fabricated. The stray magnetic fields were generated from Co edges. This technique can also be applied to other ferromagnetic materials such as Fe and Ni. Particularly, NiFe alloy is an excellent material for magnetic electrodes of spintronic devices or magnetic soft/hard materials due to its large magnetization, high controllability of spin transports, and long-term stability in air. From such perspective, $Ni_{78}Fe_{22}$ thin films sandwiched between LSP glasses were fabricated using the above technique, and their structural and magnetic properties were investigated (Chapter 3). As a result, LSP-glass/$Ni_{78}Fe_{22}$/LSP-glass structures with smooth and clear interfaces were successfully fabricated. The coercivity of $Ni_{78}Fe_{22}$ thin films was drastically enhanced from 0.9 to 103 Oe after thermal pressing at 1.0 MPa. According to the TEM and TED observations, XRD measurements, and theoretical calculations based on the random anisotropy model, this coercivity enhancement was explained by the increase in crystal grain size with random magnetic anisotropy. A uniform stray magnetic field was also observed at the $Ni_{78}Fe_{22}$ thin-film edge in the direction perpendicular to the cross section of the LSP-glass/$Ni_{78}Fe_{22}$/LSP-glass structures.

Next, $Ni_{78}Fe_{22}/Alq_3/Ni_{78}Fe_{22}$ nanoscale junctions were fabricated, and their electrical properties, such as the $Ni_{78}Fe_{22}$ electrode resistance and *I*–*V* characteristics, were investigated (Chapter 4). As a result, the formation of $Ni_{78}Fe_{22}/Alq_3/Ni_{78}Fe_{22}$ nanoscale junctions with areas of $S = 11\times11$ nm^2 was successfully demonstrated. The *I*–*V* curves obtained for these nanoscale junctions exhibited the ohmic behavior, which suggested the formation of multiple quantized conductance channels under the ballistic regime. On the other hand, The *I*–*V* curves obtained for the microscale junctions exhibited the SCLC under the diffusive scheme. In addition, the transition region between the ballistic regime and the diffusive scheme was observed for the obtained *R*–*S* plot, in which the characteristic line connecting these areas exhibited a linear correlation. This region can be considered a bridging area between the quantum states and classical configurations. Such behaviour was observed for molecular systems for the first time in this study.

In conclusion, the new developed fabrication technique to realize the molecular nanojunction utilizing thin-film edges can potentially open up opportunities not only for discovering new physical and/or chemical phenomena in nanoscale and microscale systems but also for the creation of next-generation nanodevices, including novel spin devices.

Acknowledgments

I would like to express my sincere gratitude to Prof. Junji Nishii for his continuous encouragement and valuable suggestions throughout this study. I would also like to extend my sincere gratitude to my supervisor, Prof. Hideo Kaiju for his instructive guidance and useful suggestions on my research. His guidance helped me in all the time of research and writing of this thesis. I would like to thank Prof. Masaya Fujioka for helpful advices on experiments and presentations.

I would also like to express deep acknowledgment to Prof. Yukio Hinatsu, Prof. Kei Murakoshi and Prof. Toshihiro Shimada for their valuable discussion and helpful suggestions.

I acknowledge Prof. Takashi Komine (Ibaraki University) for his supports for the calculation of the stray magnetic field in SQC devices. I also appreciate Prof. Tomoyuki Akutagawa and Prof. Norihisa Hoshino (Tohoku University) for their supports for the estimation of electronic state of Alq_3 by DFT calculation. I would like to thank Prof. Yasutaka Matsuo, Haruya Kasa, Takao Ohta, Yasushi Hirata, Masashi Takei, Koh Ohnishi and Naomi Hirai in Research Institute for Electronic Science, Hokkaido University, for their excellent technical assistance. I would like to take this opportunity to thank for all the colleagues of the Laboratory of Nanostructured Functional Materials. In particular, Sumito Mori greatly supported me in the establishment of experimental method of this study.

Finally, I would like to express my greatest gratitude to my family for their kind understanding and hearty support.

February, 2017

Takahiro Misawa